International Journal of Mass Spectrometry 274 (2008) 30–47

Contents lists available at ScienceDirect

International Journal of Mass Spectrometry

journal homepage: www.elsevier.com/locate/ijms

RF-driven ion–ion long-range interaction in a new open cylindrical ICR cell

Basem Kanawati*, Karl-Peter Wanczek[1]

Department of Physical and Inorganic Chemistry, University of Bremen, Bremen, Germany

ARTICLE INFO

Article history:
Received 17 October 2007
Received in revised form 18 April 2008
Accepted 21 April 2008
Available online 4 May 2008

Keywords:
FT-ICR
Ion–ion interaction
RF-driven overlap
Axial radial ion motion

ABSTRACT

Several approaches have been implemented to study ion–ion interactions of singly charged positive and negative ions in a new open five sectional cylindrical ICR cell with an unusual geometry, capable to trap and detect both positive and negative ions in different axial regions simultaneously. Single shot experiments, which were initially done in an attempt to achieve ion–ion interactions, did not lead to neutralization of the reactant ions, therefore RF pulse and pulse sequences with different shapes, frequencies and durations were implemented to establish longer axial overlaps between positive and negative ions in a shared central region. These RF-driven ion–ion spatial overlaps are discussed in detail in this article. Specific characteristic behaviours of the new ICR cell have been also studied.

1. Introduction

Several ICR [1] cell geometries [2] were introduced previously in the literature and used for studying charged particles under magnetic and electric fields. Open cylindrical ICR cells are more advantageous than closed ones. This is due to several reasons:

- Compatibility with external ion sources such as MALDI and electrospray ion source.
- More pumping efficiency.
- The axial component of the radial dipolar RF electric field, used for ion excitation before detection, is very low in open cell geometries compared with closed ones, since the equipotential contours of this electric filed are nearly parallel to the magnetic field lines along the *z*-axis in a wide axial region of the open ICR cells. This reduces possibility of axial ion ejection during excitation event in open cells.

On the other hand, trapping ring electrodes in open cell geometries produce approximately only one-third of the effective potential value in the center of each trapping ring electrode, compared to closed cells. This reduced effective potential has to be compensated by application of higher trapping voltages. The new ICR cell geometry, discussed in this paper, has trapping electrodes of smaller diameter than the center electrode. It combines most of the benefits of open ICR cell geometries without reducing the effective trapping potential on the terminal ends of the ICR cell to a large extent. The new characteristic features are discussed in this paper.

Simultaneous trapping of positive and negative ions were previously demonstrated in closed [3] and open ICR cells. Both static [4,5] and dynamic [6–8] electric fields were employed in double well potential configurations.

Although RF axial electric field was previously used to establish a shared stability region for trapping both ion polarities simultaneously, this axial RF electric field reduces ion detection efficiency, since this alternating electric field has also to be applied during the radial excitation event, if both ion polarities should be detected simultaneously. This induces unfavored noise in the detection circuit, although cyclotron frequencies for low m/z ions are much higher than frequencies used in the axial electric field. In high mass detection this issue would be a concern, that required installing frequency filters to reduce the trapping electric field and its RF harmonics, which are accumulated in the transient of the detection circuit.

In this article, a combined static and dynamic axial electric field was developed and implemented in the new ICR geometry to achieve the following:

- To trap simultaneously positive and negative ions in separate regions within detection area through a static double hill potential configuration.

---

* Corresponding author. Current address: Helmholtz Center Munich, Institute of Ecological Chemistry, Ingolstädter Landstraße 1, D-85764 Neuherberg, Germany. Tel: +49 89 3187 2412.

E-mail addresses: kanawati@t-online.de, Kanawati.B@gmail.com (B. Kanawati), icrwan@icr.uni-bremen.de (K.-P. Wanczek).

URL: http://www.kanawati.de (B. Kanawati).

[1] Address reprint requests to: Institute of Physical and Inorganic Chemistry, University of Bremen, FB 2, Leobener Str. NW 2, D-28334 Bremen, Germany.

1387-3806/$ – see front matter © 2008 Elsevier B.V. All rights reserved.
doi:10.1016/j.ijms.2008.04.025

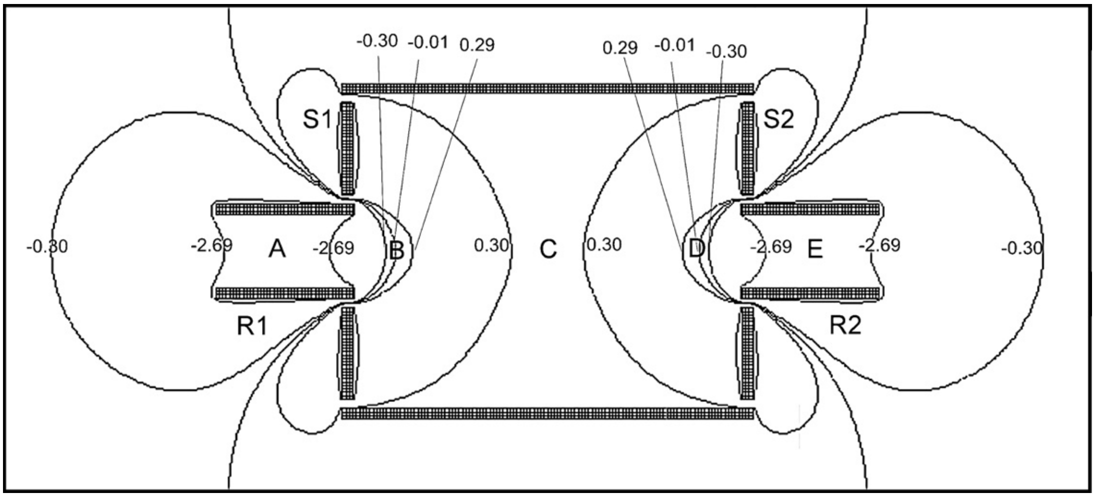

Fig. 1. Isopotential contours on the *yz*-plane in the potential configuration −3/3/0/3/−3. This cell has five different regions for trapping positive and negative ions, since the cell is located in a grounded ICR tube (not shown here). However detection is possible only inside the regions B–D.

- To establish ion–ion axial overlap by using a pulsed axial alternating electric field for a specific duration.
- To simultaneously detect both ion polarities without the presence of the axial RF electric field, so that no noise from an external RF source is added to the transient, acquired by the detection circuit.

In this context, several waveforms, with different frequencies, amplitudes and durations were used to study the efficiency of ion–ion overlap and to investigate the possibility of any type of experimental ion–ion interaction induced due to such an overlap. The search for ion–ion interactions is very important, since no ion–ion reaction was observed in ICR conditions to date, although a lot of them were observed in flowing after glow [9,10] and ion beam [11–14] techniques in addition to those observed in Paul quadrupole [15–17] ion traps.

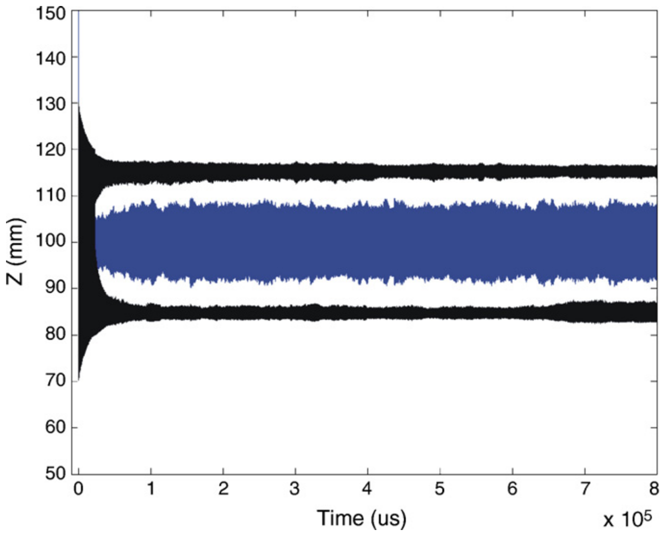

Fig. 2. SIMION simulation of 25 positive ion clouds (SF_5^+) and 25 negative ion clouds (SF_6^-) in the double well potential configuration −3/3/0/3/−3 with a total columbic charge of 4×10^{-16} C for 800 ms. Thus, nearly 2000 ions from each polarity are simulated with a damping constant of 1×10^{-4}. Positive ions are trapped in the center Z (90–110 mm), whereas negative ions are trapped at both sides 110–120 and 80–90 mm simultaneously. The axial range 50–150 mm represents the whole length of the ICR cell.

SIMION [18] simulations were done to track the movement of positive and negative ions trapped simultaneously in a static double hill potential configuration in this new ICR design in the absence and presence of gated axial RF electric field.

2. Experimental

For all experimental investigations a prototype FT-ICR spectrometer Bruker CMS47X was employed, equipped with a 7 T superconducting magnet with 89 mm room temperature bore and an Aspect 3000 computer. A UHV system connected with two fine vacuum gas inlet systems at base pressures of 3×10^{-2} mbar was used. With a turbo molecular pump of 240 L/s connected to a rotary pump a base pressure of 1×10^{-9} mbar can be reached. The sample pressure was kept constant at 2×10^{-7} mbar at all experiments.

The cell and all its geometric parameters have been described previously elsewhere [19]. Here only a brief description of the operation parameters is mentioned. The cell has two terminal tube electrodes and two side electrodes (see below). The cell has the ability to trap both positive and negative ions in different stability regions by applying a static double hill potential configuration.

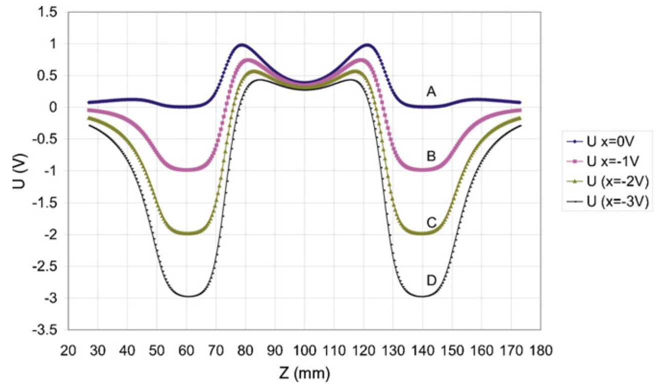

Fig. 3. Axial progression of potential along the whole length of the ICR cell in the *z*-direction for the potential configuration *x*/3/0/3/*x*, where *x* is the potential of both tube electrodes R1 and R2. (A) *x* = 0 V, (B) *x* = −1 V, (C) *x* = −2 V, and (D) *x* = −3 V. These tubes are located in the regions 50–70 and 130–150 mm. The detection area is located in the region 70–130 mm. All potential curves tend to reach 0 V outside the ICR cell, since the cell is surrounded with a grounded tube with inner diameter of 82 mm.

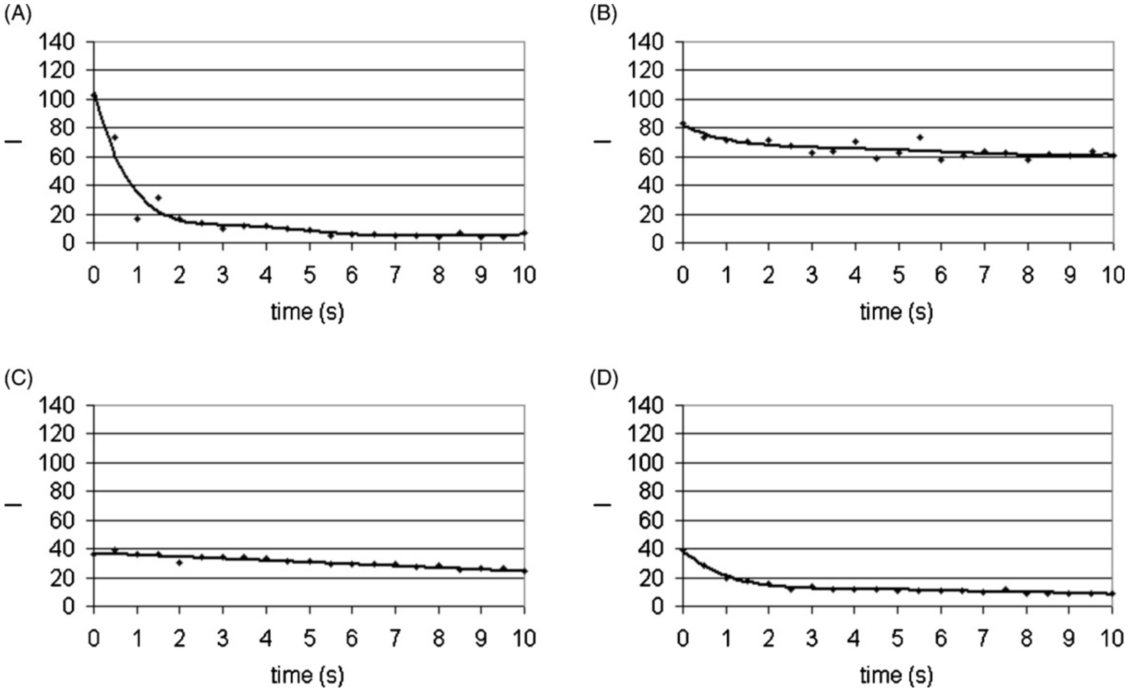

Fig. 4. Dependence of ion signal intensity on the duration of an axial RF pulse. All figures are scaled. (A) I(SF_5^+) trapped with other minor positive ions and traces of SF_5^- (Experiment I). (B) SF_5^+ trapped together with SF_6^- and all other ions (SF_5^-, SF_4^+, SF_3^+, SF_2^+) (Experiment III). (C) SF_6^- trapped alone without positive ions (Experiment II). (D) SF_6^- trapped with all other positive and negative ions (Experiment III). Solid lines are fourth- and fifth-order fitting polynomials.

The potential configuration −3/3/0/3/−3 means that terminal tube electrodes have −3 V and the internal side electrodes have +3 V relative to the central grounded region.

Ions are generated inside the ICR cell by emitting electrons with kinetic energy of 70 eV for a pulse duration of 50 ms at a current of 1.8 μA. Electrons are emitted from a rhenium filament and they fly along the magnetic field lines to enter the cell (electron movement along the *z*-axis). At these settings no space charge effects were observed. At higher ion numbers space charge effects could be detected.

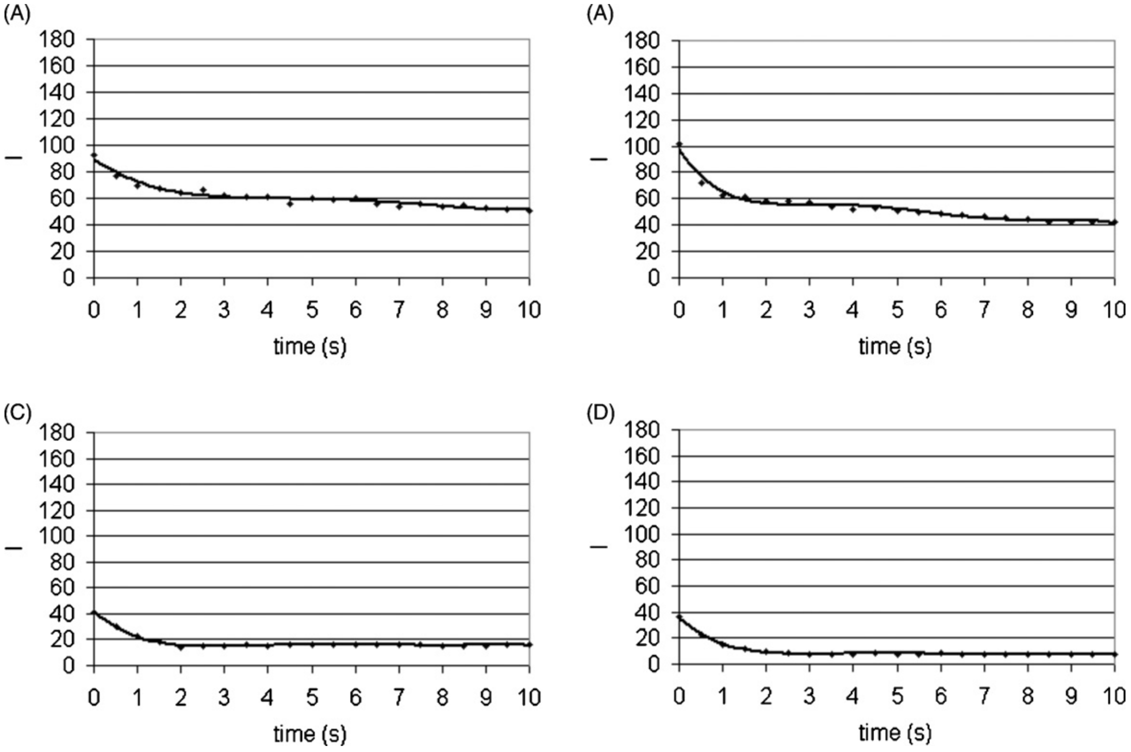

Fig. 5. Dependence of ion signal intensity on the duration of an axial RF pulse. Same scale as Fig. 4. (A) I(SF_5^+) trapped with other minor positive ions and traces of SF_5^- (Experiment I). (B) SF_5^+ trapped together with SF_6^- and all other ions (SF_5^-, SF_4^+, SF_3^+, SF_2^+) (Experiment III). (C) SF_6^- trapped alone without positive ions (Experiment II). (D) SF_6^- trapped with all other positive and negative ions (Experiment III). Solid lines are fourth- and fifth-order fitting polynomials.

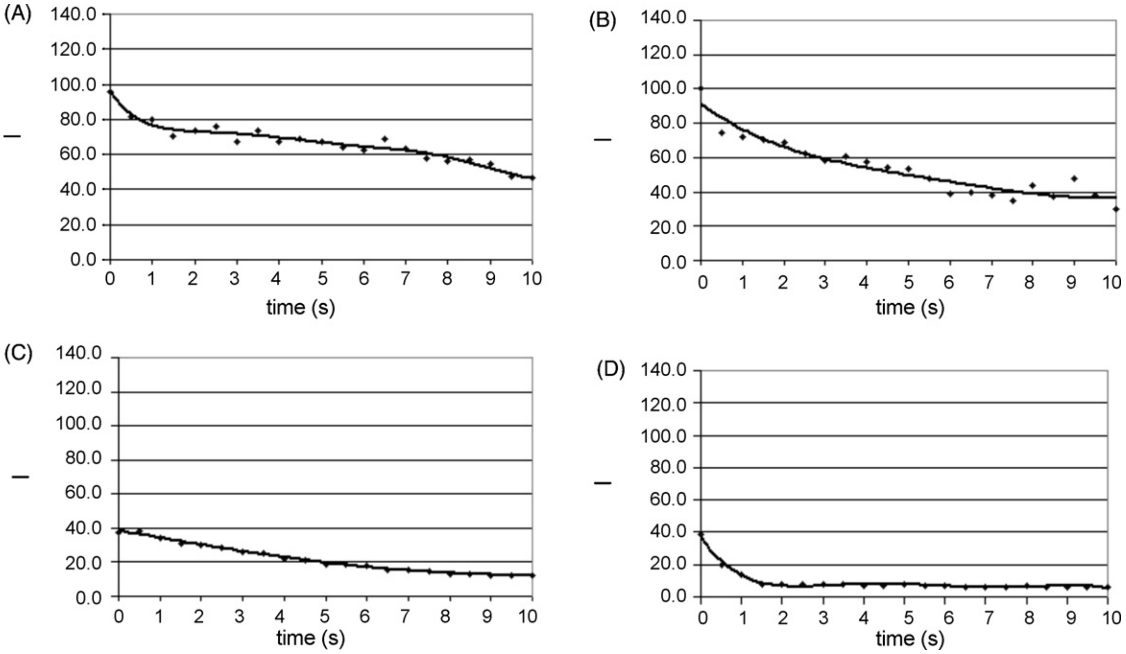

Fig. 6. Dependence of ion signal intensity on the duration of an axial RF pulse. Same scale as Fig. 4. (A) I(SF_5^+) trapped with other minor positive ions and traces of SF_5^- (Experiment I). (B) SF_5^+ trapped together with SF_6^- and all other ions (SF_5^-, SF_4^+, SF_3^+, SF_2^+) (Experiment III). (C) SF_6^- trapped alone without positive ions (Experiment II). (D) SF_6^- trapped with all other positive and negative ions (Experiment III). Solid lines are fourth- and fifth-order fitting polynomials.

Tube electrodes R1 and R2 (Fig. 1) were kept at −3 V at all experiments employing two separately programmable DAC channels. Side electrodes S1 and S2 were kept at +3 V DC offset during the experiments. Either a sinusoidal waveform (Sections 3.2.1 and 3.2.2) or a square waveform (Sections 3.2.3 and 3.3) was gated with an external Wavetek waveform generator and applied on both side electrodes. For all applied on-resonance sine waves on side electrodes (Sections 3.2.1 and 3.2.2), the wave amplitude was 0.4 Vp-p.

In Section 3.3, two off-resonant square waveforms applied on both side electrodes with frequencies 16 and 100 kHz were examined individually. Both waves have amplitude of 2 Vp-p. Alternating electric potential on both side electrodes was between +3 and +1 V in phase since both side electrodes were connected to the same Wavetek channel. Thus, axial ion excitation done by (in phase) alternating electric potential on both side electrodes has a quadrupolar character and all resonances of excitation discussed later in this study are parametric.

After the end of the RF pulse, side electrodes turned back to their initial potential +3 V again.

So the potential configuration varies in the following manner:

$$-3/3/0/3/-3 > -3/1/0/1/-3 > -3/3/0/3/-3$$

An automation program for the Aspect 3000 computer was written to control the experimental events. The logical sequence of this program is

1. Zero memory.
2. A radial frequency chirp to cover the frequency range equivalent to m/z values from 17 to 300 to eject all ions. This chirp was triggered on the excitation plates.
3. Ionization pulse for 50 ms at electron energy of 70 eV and constant electron current of 1.8 μA.
4. Post-ionization delay time of 100 ms.
5. Radial quench pulse to remove unwanted ions from the cell.
6. Trigger TTL pulse, transferred from the console to the waveform generator to start a specific RF pulse.
7. Delay time of 100 ms after the end of the TTL pulse.
8. Radial dipolar excitation pulse for ion detection.

Pure SF6 gas was used for all experiments. This gas was purchased from Messergroup and used without any further purification. At a pressure of 2×10^{-7} mbar the post-ionization delay time of 100 ms was sufficient to thermalize the remaining electrons by

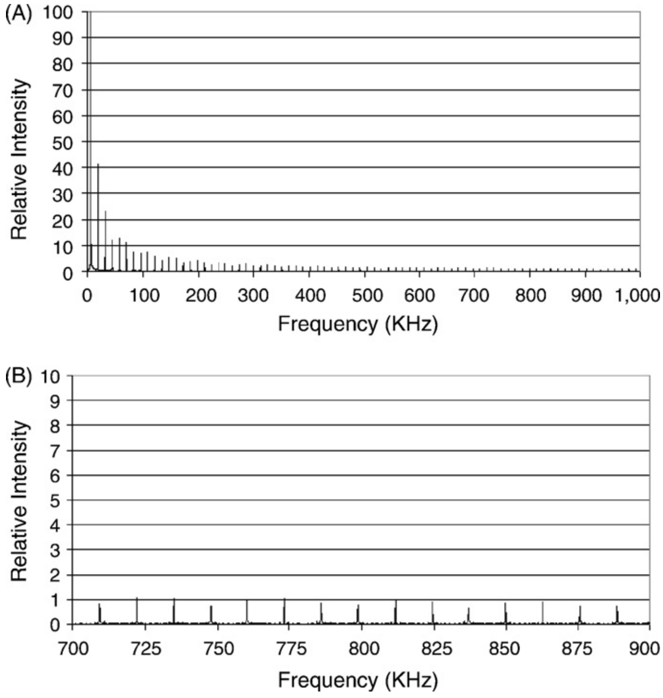

Fig. 7. (A) Frequency components of a square waveform of frequency 6391 Hz after Fourier transform with a sampling rate of 8 MHz and 64K data points. (B) Enlarged segment of the upper diagram in the range 700–900 kHz.

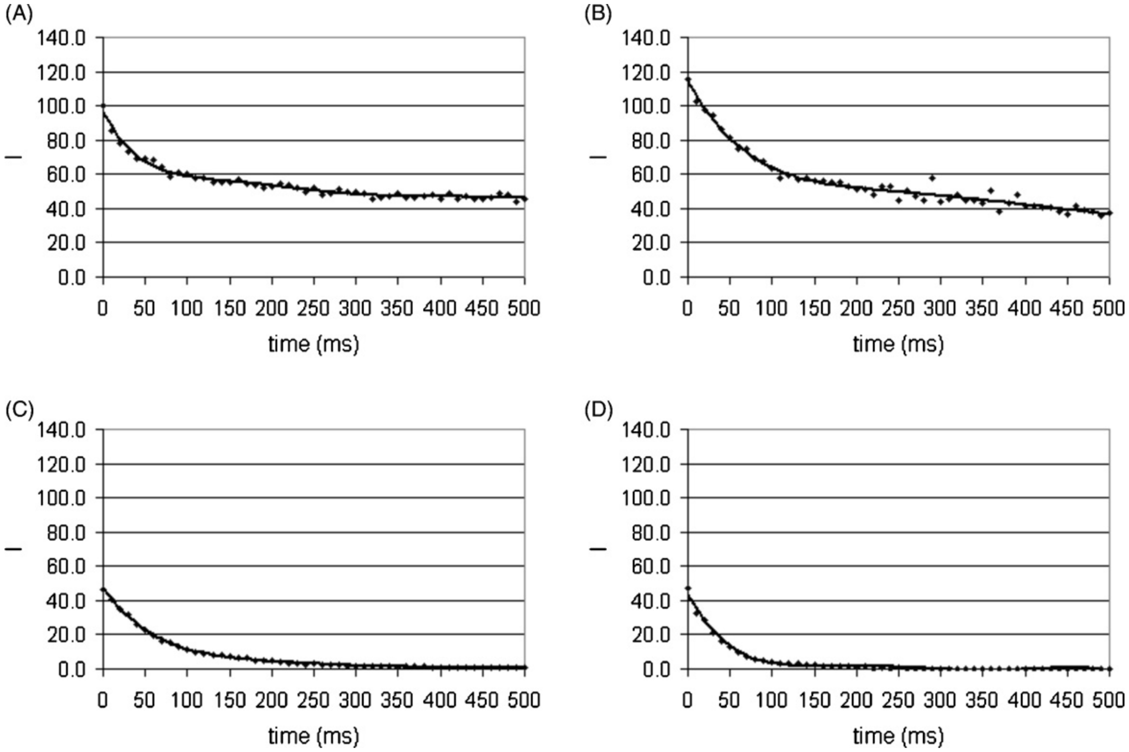

Fig. 8. Dependence of ion signal intensity on the duration of an axial RF pulse. (A) I(SF_5^+) trapped with other minor positive ions and traces of SF_5^- (Experiment I). (B) SF_5^+ trapped together with SF_6^- and all other ions (SF_5^-, SF_4^+, SF_3^+, SF_2^+) (Experiment III). (C) SF_6^- trapped alone without positive ions (Experiment II). (D) SF_6^- trapped with all other positive and negative ions (Experiment III). Solid lines are fourth- and fifth-order fitting polynomials.

collisions with the neutral molecules and to attach electrons to SF_6 to form SF_6^- and a small fraction of SF_5^- ions. With the negative only mode and the potential configuration −3/−3/0/−3/−3 the relative intensity of the SF_5^- ions was 3% of SF_6^-.

The waveform generator was set up to work in gated mode, which means that the RF pulse applied from the waveform generator had the same duration of the triggered TTL pulse, which was transferred from the main console to the waveform generator. The ICR cell has high trapping efficiency (>15 s) for both positive and negative ions in the studied −3/3/0/3/−3 double well potential configuration at 5×10^{-7} mbar.

3. Results and discussions

3.1. Description of ion trajectories and potential contours of the ICR cell in a static trapping electric field

The *yz*-midplane geometry of the new ICR cell is shown in Fig. 1. R1 and R2 are two stainless steel tubes with an inner diameter of 10 mm. Each tube electrode is 20 mm long. The side electrodes (S1 and S2) have a circular geometry with a bore in the center of each side electrode, in which the tube electrodes R1 and R2 fit. The inner length of the ring electrodes between S1 and S2 is 60 mm. The ring electrodes consist of eight stainless steel segments. Two opposite pairs of adjacent segments are employed for excitation and detection. The inner diameter of the ICR cell is 46 mm. The whole ICR cell assembly is placed in the grounded stainless steel tube of the ICR vacuum system with an inner diameter of 82 mm.

Fig. 1 also shows the equipotential contours in the potential configuration −3/3/0/3/−3. The narrow stability regions B and D are suitable for trapping negative ions, while the broad region C created in −3/3/0/3/−3 is suitable for trapping positive ions. Note the potential flatness on the wide detection region of the ICR cell.

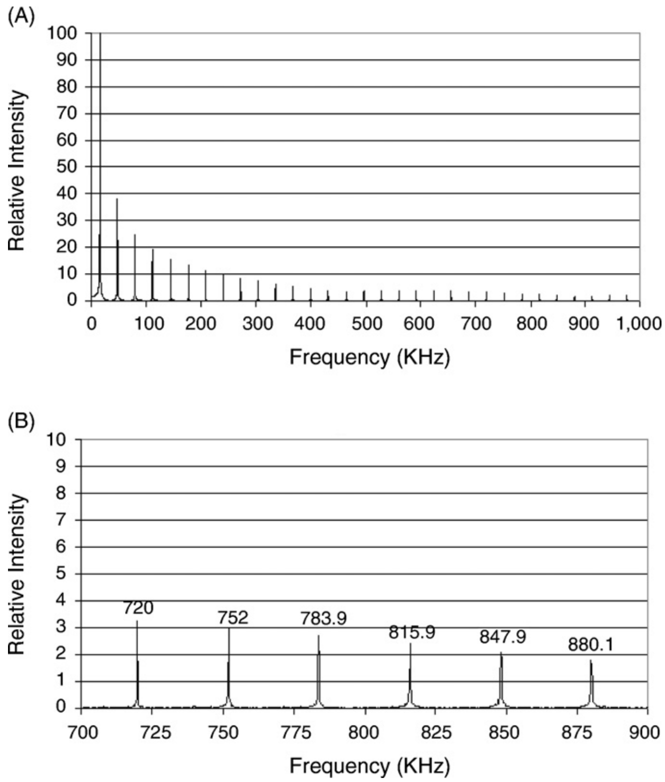

Fig. 9. (A) Frequency components of a square waveform of frequency 16 kHz after Fourier transform with a sampling rate of 16 MHz and 64K data points. (B) Enlarged segment of the top diagram in the range 700–900 kHz.

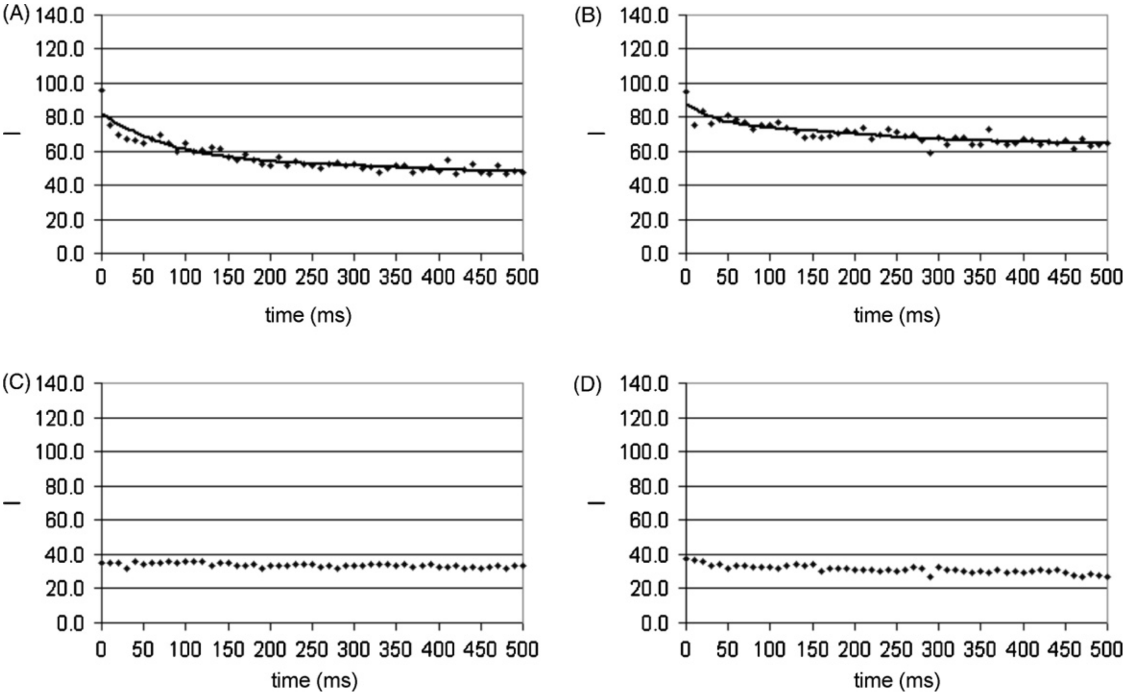

Fig. 10. Dependence of ion signal intensity on the duration of an axial RF pulse. Same scale as Fig. 8. (A) I(SF_5^+) trapped with other minor positive ions and traces of SF_5^- (Experiment I). (B) SF_5^+ trapped together with SF_6^- and all other ions (SF_5^-, SF_4^+, SF_3^+, SF_2^+) (Experiment III). (C) SF_6^- trapped alone without positive ions (Experiment II). (D) SF_6^- trapped with all other positive and negative ions (Experiment III). Solid lines are fourth- and fifth-order fitting polynomials.

Fig. 2 shows a SIMION simulation for the trapped SF_5^+ and SF_6^- with damping [20] and columbic repulsion considerations for 800 ms on the potential configuration −3/3/0/3/−3. As can be seen from Fig. 2, simultaneous trapping of both positive and negative ions in different sites of the ICR cell is possible.

The use of time varying electric field is an attempt to establish an overlap between positive and negative ions in the central region of the ICR cell. Other methods published by the same authors [21] have been also suggested to bring positive and negative ions to overlap axially in the central region of the ICR cell. RF-driven overlap is discussed in the next section.

As seen from Fig. 2, positive ions can be trapped in a wide range in the center of the ICR cell (region C), whereas negative ions have two stable regions, located at B and D of the cell, both inside the detection region. So both polarities can be excited and detected simultaneously. Terminal ions face a strong axial component of the radial excitation electric field [19] which leads some of these ions to collide with inner surfaces of the side electrodes S1 and S2.

Fig. 3 shows different axial potential courses along z-direction as a function of the applied potential of each tube electrode when both side electrodes are kept at +3 V in all demonstrated curves. From this figure, it is clear that the potential configuration, established by R1 = R2 = −3 V makes the potential configuration very flat in the central region, while negative ions are strongly pushed toward the inner central region of the ICR cell because of the relatively high negative potentials at both tube electrodes ($x = -3$) as compared to lower values ($x = -2$, -1 and 0 V). This flat potential configuration in the center of the ICR cell caused by −3/3/0/3/−3 is responsible for the large trapping amplitude of central positive ions as seen in Fig. 2. On the other hand, negative ions in the same potential configuration are confined in narrow axial regions (B and D) because the potential in each terminal region is much narrower, as compared with the flat central well. This is in agreement with the equipotential contours shown in Fig. 1.

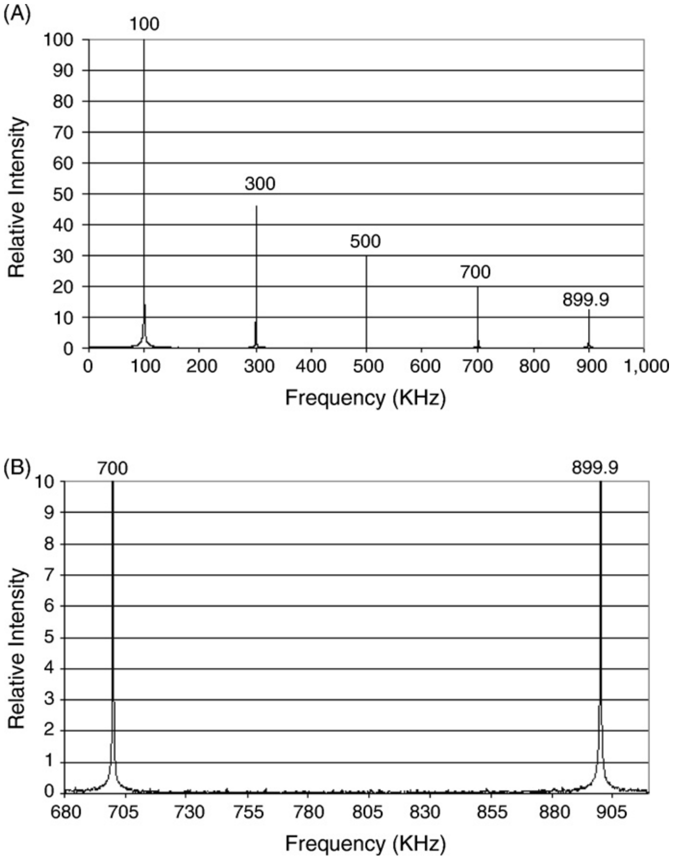

Fig. 11. (A) Frequency components of a square waveform of frequency 100 kHz after Fourier transform with a sampling rate of 16 MHz and 64K data points. (B) Segment of the top diagram in the range 680–920 kHz.

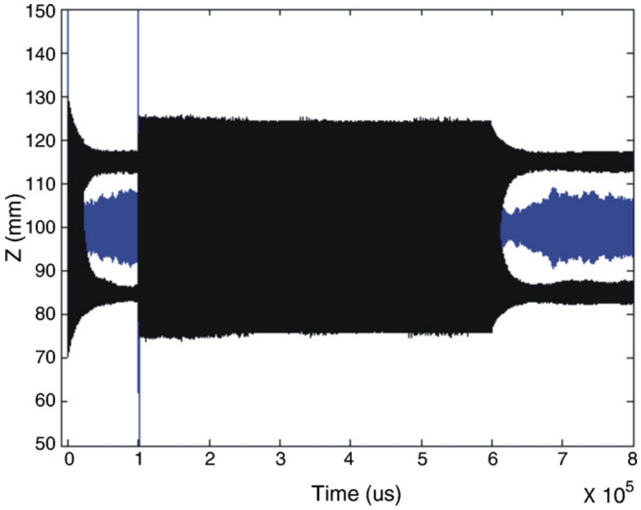

Fig. 12. Axial trajectories of thermal positive ($m/z = 127$) and negative ($m/z = 146$) ions versus time with axial square waveform RF pulse of frequency 16 kHz. Wide axial overlap between central positive ions and terminal negative ions are shown.

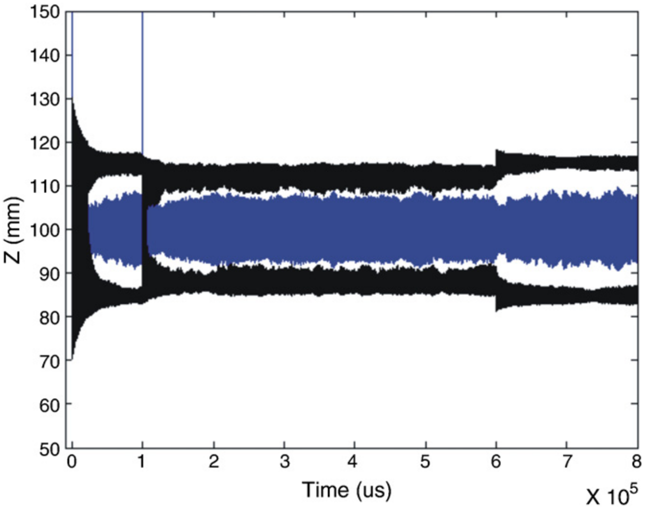

Fig. 13. Axial trajectories of thermal positive ($m/z = 127$) and negative ($m/z = 146$) ions versus time with axial square waveform RF pulse of frequency 100 kHz. Positive ions are trapped in the central region, while negative ions are trapped in both terminal regions.

Note also the displacement of the maxima of the two potential hills toward the center of the ICR cell (Fig. 3), as the potential of each tube electrode becomes more negative. This causes a possibility of ion–ion interaction shortly after ion generation before damping starts, which affects axial ion motion of both polarities exponentially as a function of time. This agrees with the simulation in Fig. 2 in the first 20 ms. In this time interval, electrons are still available for possible ion–electron recombination processes, since they exhibit much higher recombination rate coefficients in comparison with ion–ion recombination in general.

From Fig. 3 it is also worth to note the difference between the conditions, in which positive and negative ions are trapped simultaneously. While positive ions are trapped in a central symmetric flat potential well, terminal negative ions vibrate axially in a strongly asymmetric potential configuration in each stability region (regions B and D in Fig. 1), especially when the tube electrodes have high negative values such as −3 V (Fig. 3). Later we will see the impact of this difference on the trajectories of both ion polarities.

3.2. Axial RF-driven ion–ion overlap using on resonance frequencies

3.2.1. Sine waveform at a frequency 6391 Hz and amplitude 0.4 Vp-p

In this experimental investigation, the double hill potential configuration −3/3/0/3/−3 at a constant pressure of 2×10^{-7} mbar was applied. Sine waveform at a constant frequency of 6391 Hz (the calculated trapping frequency of SF_5^+) was pulsed on both side electrodes in phase with a variable pulse length from 0 to 10 s with a peak to peak voltage of 0.4 V. Three experiments were done during the application of this axial RF pulse:

Experiment I: Only positive ions produced from SF_6 gas were trapped in the center of the ICR cell. SF_6^- ions were radially quenched using a single shot RF pulse at resonance frequency. Traces of SF_5^- remained trapped in the terminal regions B and D.

Experiment II: Only SF_6^- ions, formed as a result of thermal electron attachment, were trapped in both terminal regions B and D of the ICR cell. All positive ions were radially ejected using a suitable frequency chirp, gated from the excitation plates for 100 μs at an attenuation level of 2 db (115.5 Vp-p).

Experiment III: Positive and negative ions were trapped simultaneously in the ICR cell. Positive ions remain in the central region C, while negative ions are in the terminal regions B and D.

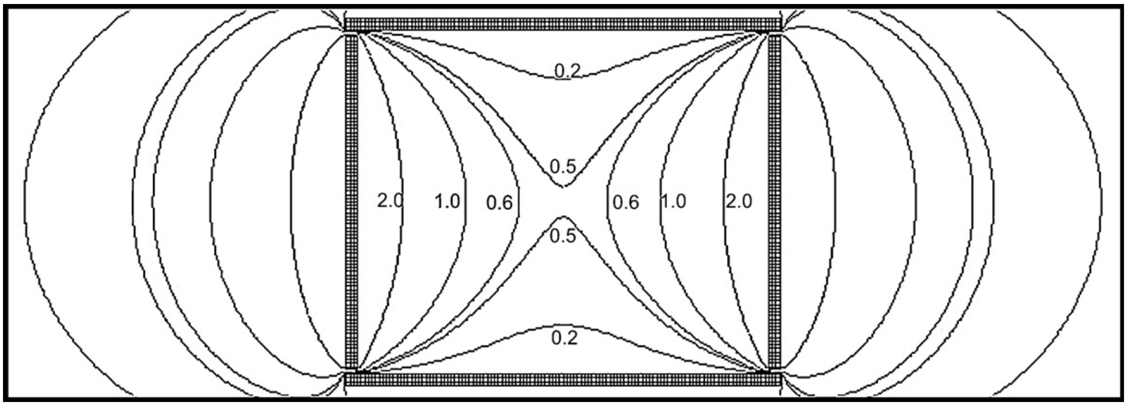

Fig. 14. Equipotential contours on the *yz*-midplane of a simple closed cylindrical ICR cell 60 mm long with inner diameter of 46 mm, and potential configuration 3/0/3.

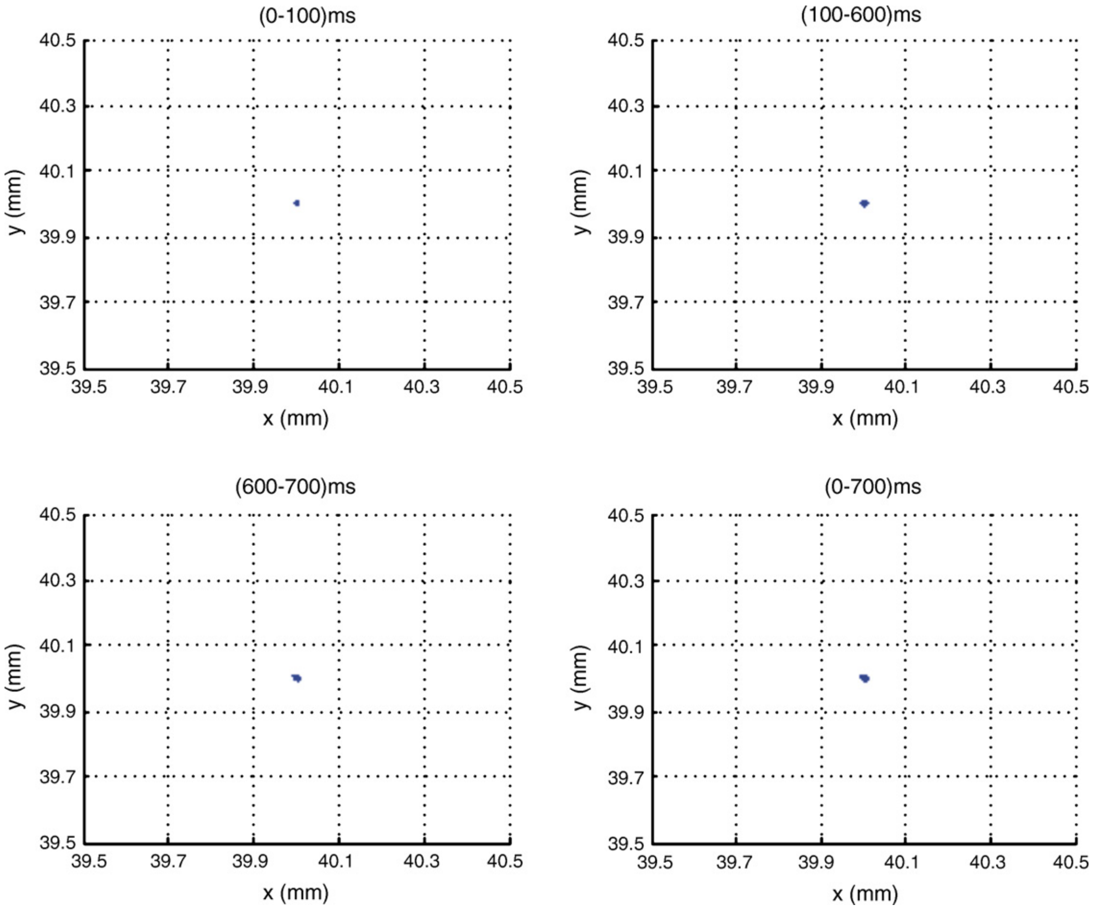

Fig. 15. Radial view of 25 thermal positive ion clouds ($m/z = 127$), simulated under columbic charge of 2×10^{-16} C and damping constant of 1×10^{-4} in a simple closed cylindrical ICR cell with potential configuration 3/0/3. Central point is located at (40, 40) in mm.

The time scale shown on each diagram of Fig. 4 and all other upcoming figures refers to the RF pulse duration. In all experiments in Section 3.2, an initial delay time of 100 ms was allowed directly after electron impact ionization to ensure that remaining electrons were thermalized and converted to anions (mainly SF_6^-). This duration time was more than sufficient at the pressure of 2×10^{-7} mbar to ensure complete absence of electrons from the ICR cell before studying ion–ion interactions. After the RF pulse, another 100 ms allow damping of axial motion, before radial excitation for detection. The same calibration is utilized in all plots.

From Fig. 4 we conclude an obvious ion–ion interaction between axially excited SF_5^+ and SF_6^- ions during the sine RF pulse at resonance trapping frequency of SF_5^+ ions. With absence of SF_6^- (Fig. 4A), the effect of axial excitation RF pulse on the axial ejection of SF_5^+ ions is much larger than with the presence of SF_6^- ions (Fig. 4B).

However, the signal intensity of terminal SF_6^- ions decreases exponentially to a lower value after 10 s duration of the axial RF pulse when SF_5^+ ions are trapped and axially excited (compare Fig. 4C with D). This may be due to ion–ion collisions without neutralization. When trapped with SF_5^+ ions, SF_6^- are lost more effectively, because of a possible ion–ion collision between the axially excited SF_5^+ and SF_6^- ions in the terminal detection regions B and D.

3.2.2. Sine waveform at a frequency 9758 Hz and amplitude 0.4 Vp-p

The same Experiments I, II, and III described in Section 3.2.1 were done here but with a different frequency, which corresponds to the simulated trapping frequency of SF_6^-, trapped at both sides of the detection regions B and D. Fig. 5 shows the results of this investigation.

Referring to Fig. 1, there is a narrow zone (region C) in which the positive ions, trapped in the center are no longer stable, if an RF pulse is going to change the potential wells generated by the side electrodes. Furthermore, off-resonance axial RF pulses increase the trapping amplitude of the positive ions, trapped in the sensitive flat narrow region C. After the end of the axial RF pulse, all positive ions with higher trapping amplitudes beyond the equipotential contours at 0.30 V in Fig. 1 can be easily ejected axially after switching off the axial RF field provided from the side electrodes and consequently returning back to the static potential configuration −3/3/0/3/−3.

A sine waveform acting for 10 s at a frequency of 9758 Hz is on resonance with the trapping frequency of SF_6^-, trapped in the terminal regions B and D, but it acts as off-resonance axial excitation pulse toward SF_5^+ ions trapped in the center (region C), since the difference in m/z values between SF_6^- and SF_5^+ ions is small. Therefore, the intensity of SF_5^+ is reduced to about the half after 10 s RF irradiation relative to the initial intensity of SF_5^+ (Fig. 5A). No reduction is observed without RF irradiation.

As shown in Fig. 5C and D, no significant difference in SF_6^- ion loss during irradiation period is observed, whether positive ions are present (Fig. 5D) or absent (Fig. 5C). This is logical because SF_6^- ions can be ejected without passing through the center of the ICR cell, where SF_5^+ ions are trapped. On the other hand, SF_5^+ ions do not remain confined in the narrow central

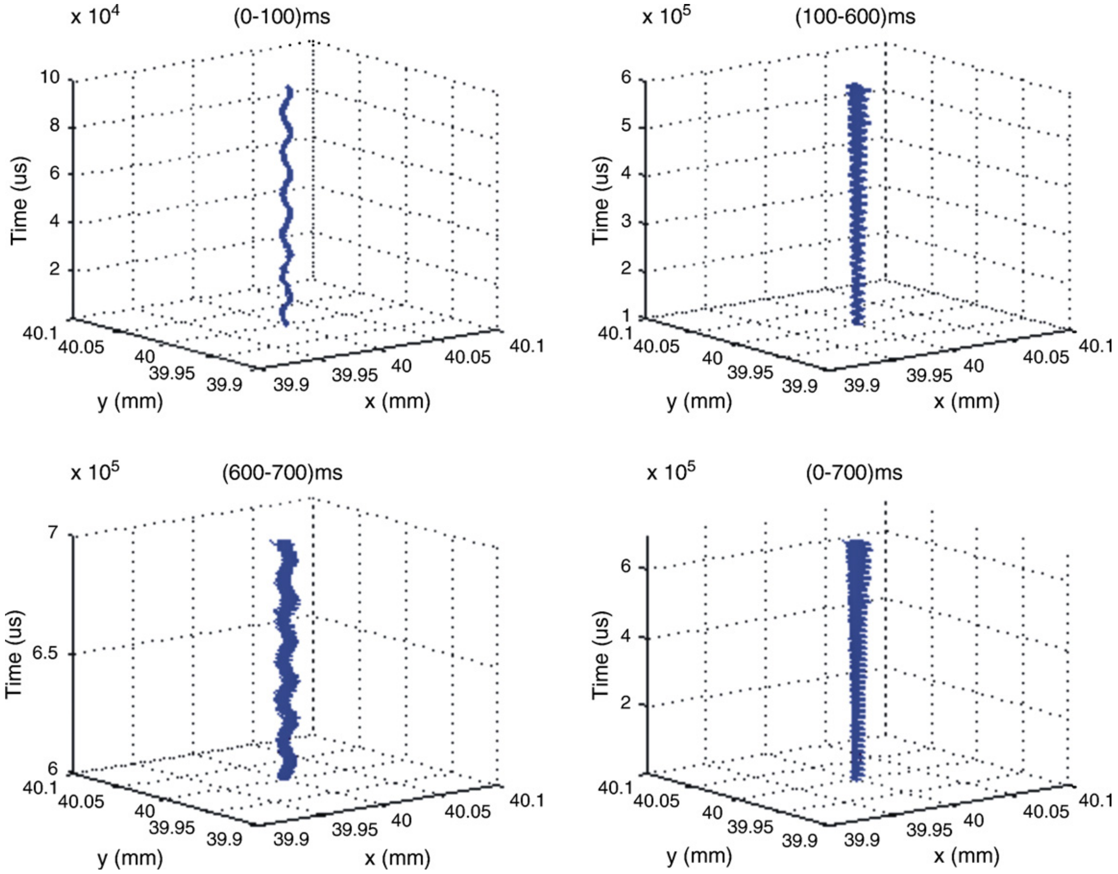

Fig. 16. Expanded 3D view of Fig. 15 for the radial confinement of 25 thermal positive ion clouds ($m/z = 127$) as a function of time.

region C and they are also affected by this axial RF pulse, which acts as off-resonance for SF_5^+ ions. Thus, axially excited (and partially ejected) SF_5^+ ions can even induce some more SF_6^- loss. This is apparent from Fig. 5C and D. Furthermore, SF_5^+ ion loss is higher in the presence of SF_6^- ions after the excitation pulse. This means that 15 units of SF_5^+ ions (compare Fig. 5A with B) were attracted within the scope of ion–ion interaction to the axially on-resonance excited SF_6^- and were mutually quenched.

3.2.3. Square waveform at frequency 6391 Hz and amplitude 0.4 Vp-p

The same three Experiments I, II, and III described in Sections 3.2.1 and 3.2.2 were done in this section at the same RF pulse amplitude 0.4 Vp-p but with a square waveform at a frequency of 6391 Hz. Square waveforms contain several useful frequency components, which can induce on-resonance and off-resonance excitation of both trapping and cyclotron motion of ions in the ICR cell simultaneously. Furthermore, SIMION simulations have indicated that application of an axial square waveform at both side electrodes in the frequency range 5–16 kHz can achieve positive–negative axial ion overlap between central positive and terminal negative ions during the whole pulse period in the double hill potential configuration −3/3/0/3/−3. Fig. 6 shows the effect of implementation of a square waveform at frequency of 6391 Hz (0.4 Vp-p) to excite central SF_5^+ ions axially in the same potential configuration −3/3/0/3/−3.

In order to correctly understand the effect of the square waveform, we have Fourier transformed the square waveform pulse of frequency 6391 Hz to obtain its real frequency components (Fig. 7).

At 7 T magnetic field, the simulated cyclotron frequency of SF_5^+ is 846.4 kHz, while that of SF_6^- is 736.3 kHz. A small frequency component exists at 735 kHz very close to the cyclotron frequency of SF_6^- ions trapped at terminal detection regions B and D. This frequency component is effective over a long period of time (10 s), in which the square waveform pulse is applied. The frequency difference of 1.3 kHz corresponds to less than 0.3 Da m/z difference. The 1% relative signal intensity of this frequency component is sufficient to induce a partial radial increase of the cyclotron frequency of SF_6^- ions, since the square waveform has a very long duration of time (up to 10 s).

Thus negative ions trapped and radially excited during the square pulse, do not interact with positive ions, which are on-resonance (and thus axially excited) with the trapping frequency of SF_5^+ ions. As a result, SF_6^- ions in Experiment III (all ions are present) do not reduce the loss of SF_5^+ ions, which are axially excited to the terminal ends of the ICR cell during the square pulse. No ion–ion collisions occur in this case.

Both investigations, described in Sections 3.2.1 and 3.2.3 lead to the same conclusion: Although it is clear that in both investigations SF_5^+ ions were on-resonance axially excited, in Section 3.2.1 (Fig. 4A and B) we observe a noticeable preservation of SF_5^+, when SF_6^- ions are trapped together with SF_5^+ ions. On the other hand, if we compare the transition Fig. 4A to B with the transition Fig. 6A to B we notice that the axial on-resonance excitation of SF_5^+ ions with a square waveform does not induce the same preservation of SF_5^+ ions, when terminal SF_6^- ions are trapped simultaneously with central SF_5^+ ions. The reason of this difference is the radial

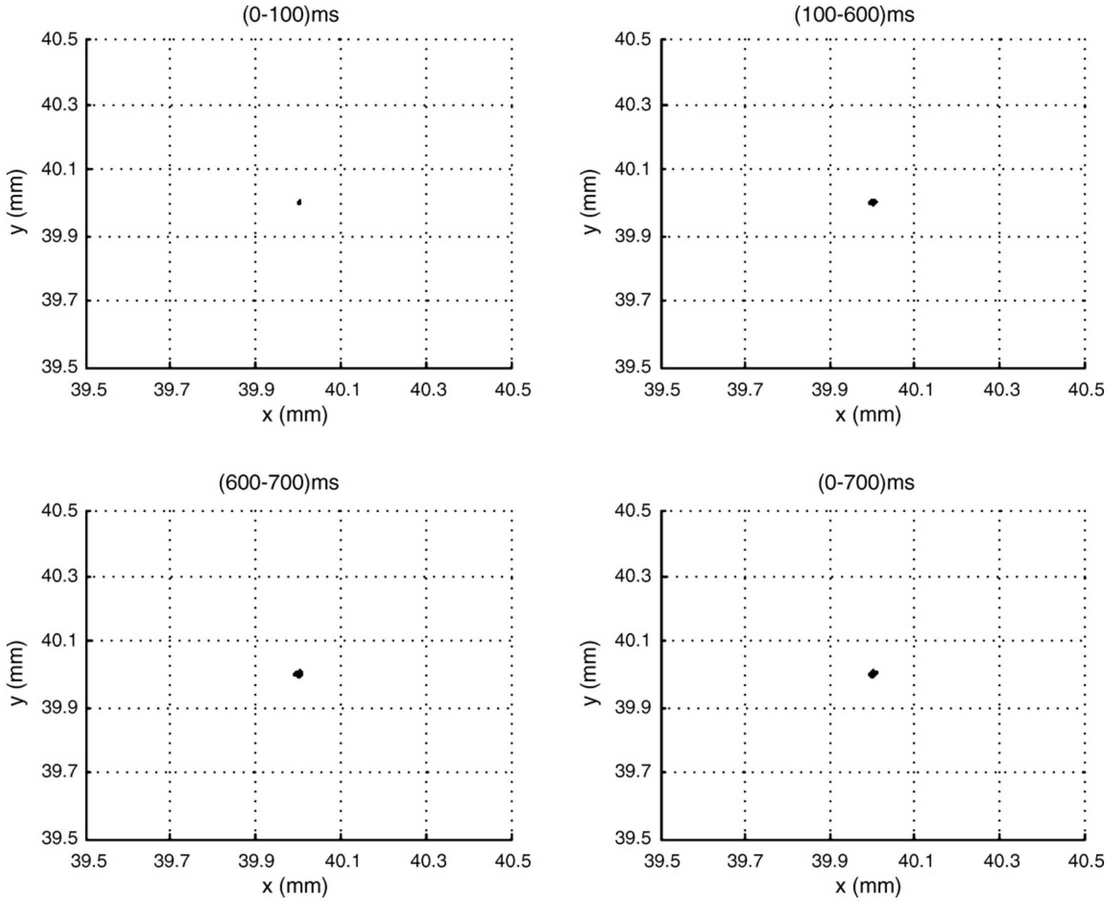

Fig. 17. Radial view of 25 thermal negative ion clouds ($m/z = 146$), simulated under columbic charge of 2×10^{-16} C and damping constant of 1×10^{-4} in a simple closed cylindrical ICR cell with potential configuration −3/0/−3. Central point is located at (40, 40) in mm.

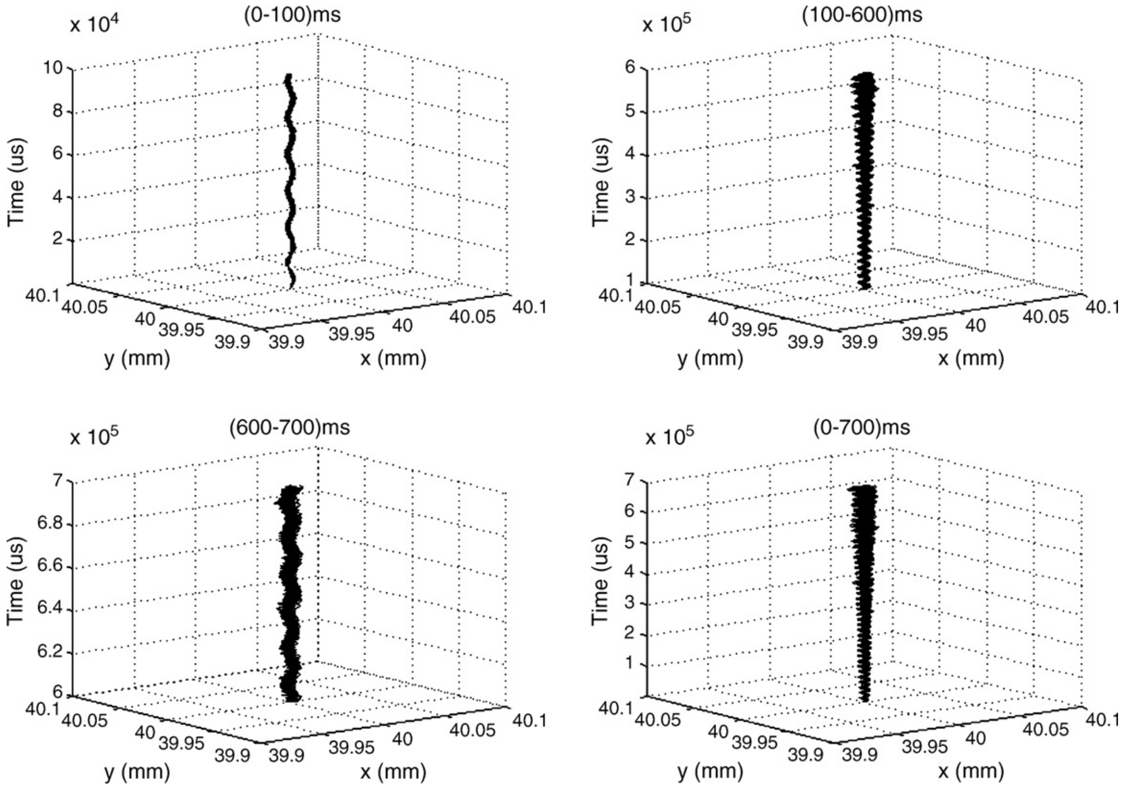

Fig. 18. Expanded 3D view for the radial confinement of 25 thermal negative ion clouds ($m/z = 146$) introduced in Fig. 17 as a function of time.

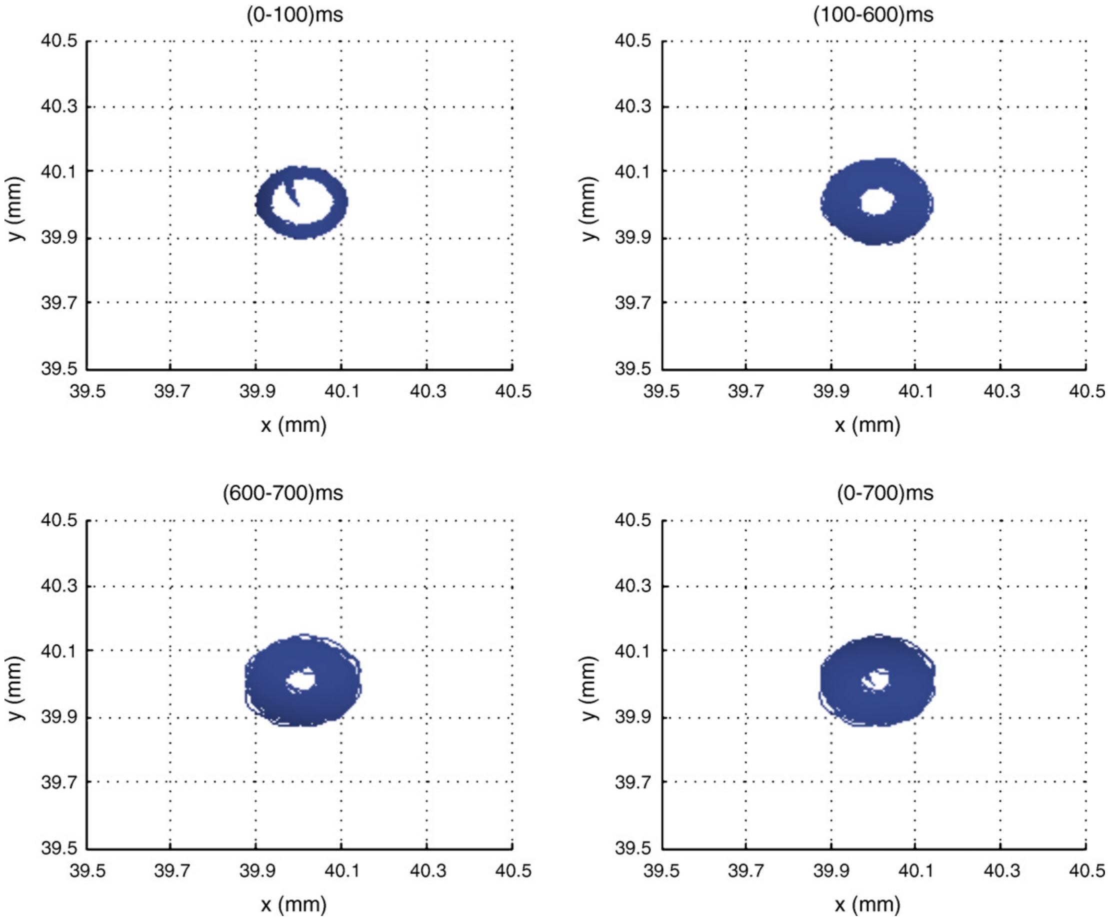

Fig. 19. Radial confinement of 25 thermal positive ion clouds ($m/z = 127$), simulated as accumulated trajectories in the range 0–700 ms in four time segments in the potential configuration −3/3/0/3/−3 of the new open cylindrical ICR cell.

frequency component at 735 kHz, which is absent in the sine waveform but present in the square waveform.

3.3. Axial RF-driven ion–ion overlap using off resonance RF frequencies

In this experimental investigation, the same double hill potential configuration −3/3/0/3/−3 was applied at a relatively high constant pressure of 2×10^{-7} mbar. Square waveforms at analog frequencies 16 and 100 kHz were generated on both side electrodes (in phase) with variable duration times ranging from 0 to 500 ms with a peak to peak voltage of 2 V. Three experiments were done during this RF pulse:

In Experiment I, only positive ions produced from SF_6 gas were trapped in the center of the ICR cell. SF_6^- ions were radially quenched using a single shot RF pulse, initiated from the excitation electrodes at resonance cyclotron frequency. Traces of SF_5^- ions remained trapped in both terminal detection regions B and D.

In Experiment II, only SF_6^- ions, formed as a result of thermal electron attachment, were trapped at both sides B and D of the ICR cell. All positive ions were radially ejected by a suitable frequency chirp in the cyclotron frequency range of unwanted ions, pulsed from the excitation plates for 100 μs at an attenuation level of 2 db (115.5 Vp-p).

In Experiment III, all ions (positively and negatively charged) were trapped together in the ICR cell. Positive ions remained in central region C, while negative ions were trapped in the terminal regions B and D.

3.3.1. Square waveform of frequency 16 kHz

SF_6^- ions were axially excited off-resonance in this experiment (Fig. 8C). Fig. 8B shows more SF_5^+ ion loss (nearly 20 units) when SF_6^- ions were trapped in the terminal detection regions B and D in comparison with the case of absence of terminal SF_6^- (Fig. 8A). This indicated a slight ion–ion interaction between SF_5^+ and SF_6^-, during the period of time, in which this axial square waveform RF pulse was applied. On the other hand, SF_6^- ions were ejected independently of the absence or presence of SF_5^+ ions, trapped in the center (compare Fig. 8C with D).

The frequency components of this square waveform of frequency 16 kHz are shown in Fig. 9A and B. The cyclotron frequency of SF_6^- ions (736.3 kHz) is surrounded by frequency components of 720 and 752 kHz. These frequency components are nearly ±16 kHz off-resonant from the cyclotron frequency of terminal SF_6^- ions. These ions are also subject to an off-resonance axial square waveform. Thus, we should expect a noticeable radial expansion of the cyclotron motion of these ions, while they are ejected using off-resonance axial pulse. SF_5^+ ions can be radially excited by this square waveform pulse to a larger extent, since a frequency component at 847.9 kHz exists, which just differs by 1.5 kHz from the cyclotron frequency of SF_5^+ ions (846.4 kHz) only. Sine waveform axial ion excita-

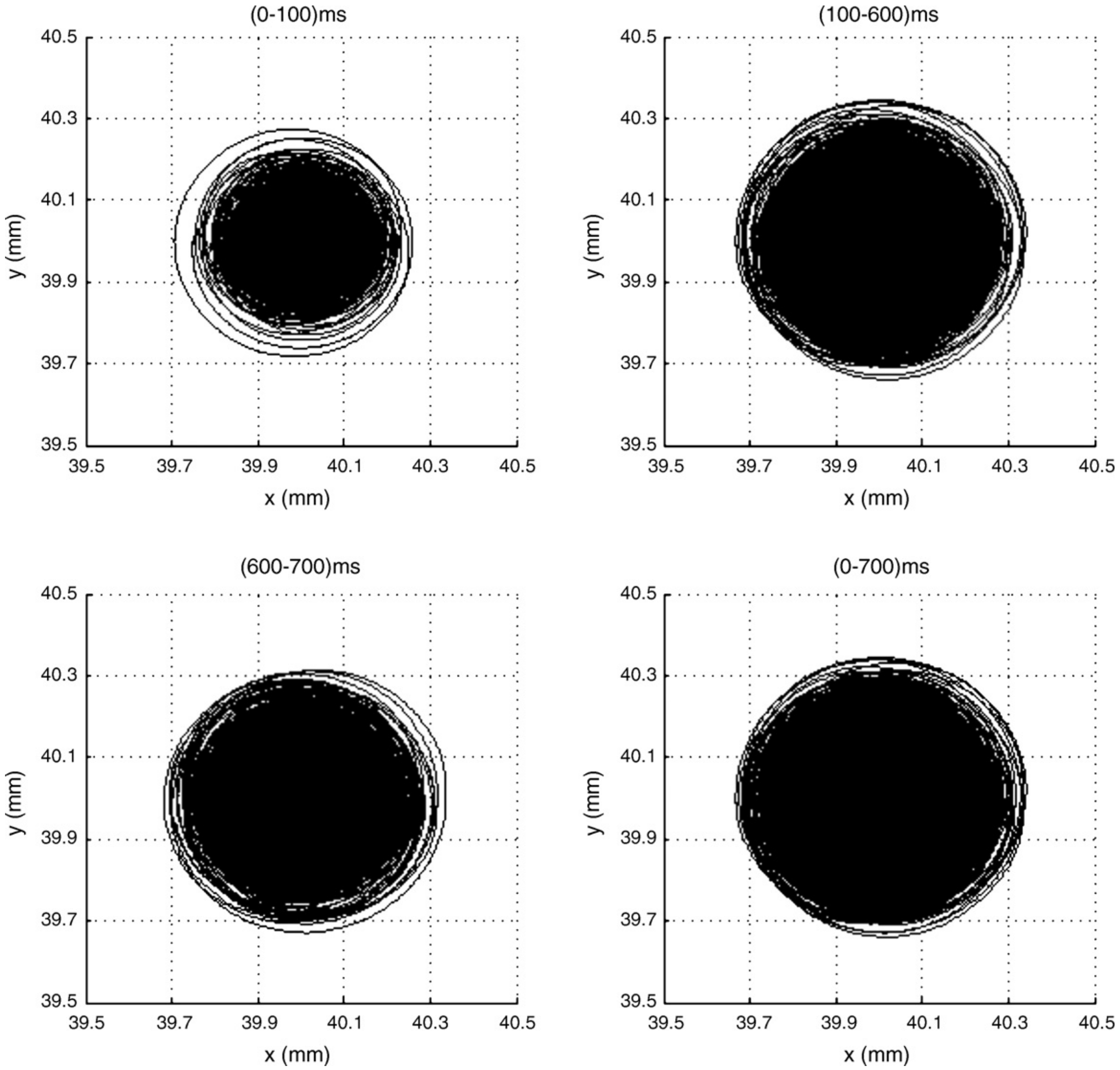

Fig. 20. Radial confinement of 25 thermal negative ion clouds (m/z = 146), simulated as accumulated trajectories for the first 700 ms time of flight in four time segments in the potential configuration −3/3/0/3/−3 of the new open cylindrical ICR cell.

tion for SF_3^+ and SF_6^- at harmonics of the used square wave with analogue frequencies of 6391 Hz and 16 kHz were also investigated, but they did not lead to any discernable ion–ion interactions.

3.3.2. *Square waveform at a frequency of 100 kHz*

At and above the frequency of 100 kHz, SF_6^- ions are not affected with the axial square waveform pulse. However, partial loss of SF_5^+ ions, trapped in the flat central potential region (cf. Fig. 1) can still be observed, as indicated in Fig. 10. With this square pulse, SF_5^+ and SF_6^- ions cannot be radially excited, since no frequency components in the cyclotron range 710–890 kHz exist (Fig. 11B).

The cyclotron frequencies of SF_5^+ and SF_6^- are 846.4 and 736.3 kHz, respectively. The following deviations from the two frequency components at 700 and 900 kHz are

$$\Delta\nu(SF_6^-) = -36.3\,\text{kHz} = -3.7\nu_z(SF_6^-),$$

$$\Delta\nu(SF_5^+) = 53.6\,\text{kHz} = +8.4\nu_z(SF_5^+)$$

These frequency deviations are too high to cause noticeable changes in the cyclotron radii of both polarities. So only axial ejection mechanism is possible for the partial loss of SF_5^+ ions as seen in Fig. 10A.

After we have ruled out any possibility of radial ejection mechanism, we can say, that the drop of SF_5^+ signal intensity is higher in the absence of SF_6^- ions, trapped in the terminal detection regions B and D compared with SF_5^+ ion loss at the presence of terminal SF_6^- ions (compare diagrams A with B in Fig. 10). This presents evidence that a long-range ion–ion interaction between both polarities without electron transfer can occur. The interaction is small with the square waveform. A much larger ion–ion interaction could be observed in Section 3.2.1, when a simple sine waveform axial pulse at 6391 Hz is applied (compare the diagrams A and B in both Figs. 10 and 4).

3.4. *SIMION simulations for axially confined thermal positive and negative ions*

Twenty-five positive ion clouds (m/z = 127) and 25 negative ion clouds (m/z = 146) were simulated in a homogenous magnetic field of 7 T and the potential configuration −3/3/0/3/−3. The total amount of columbic charge was set up to

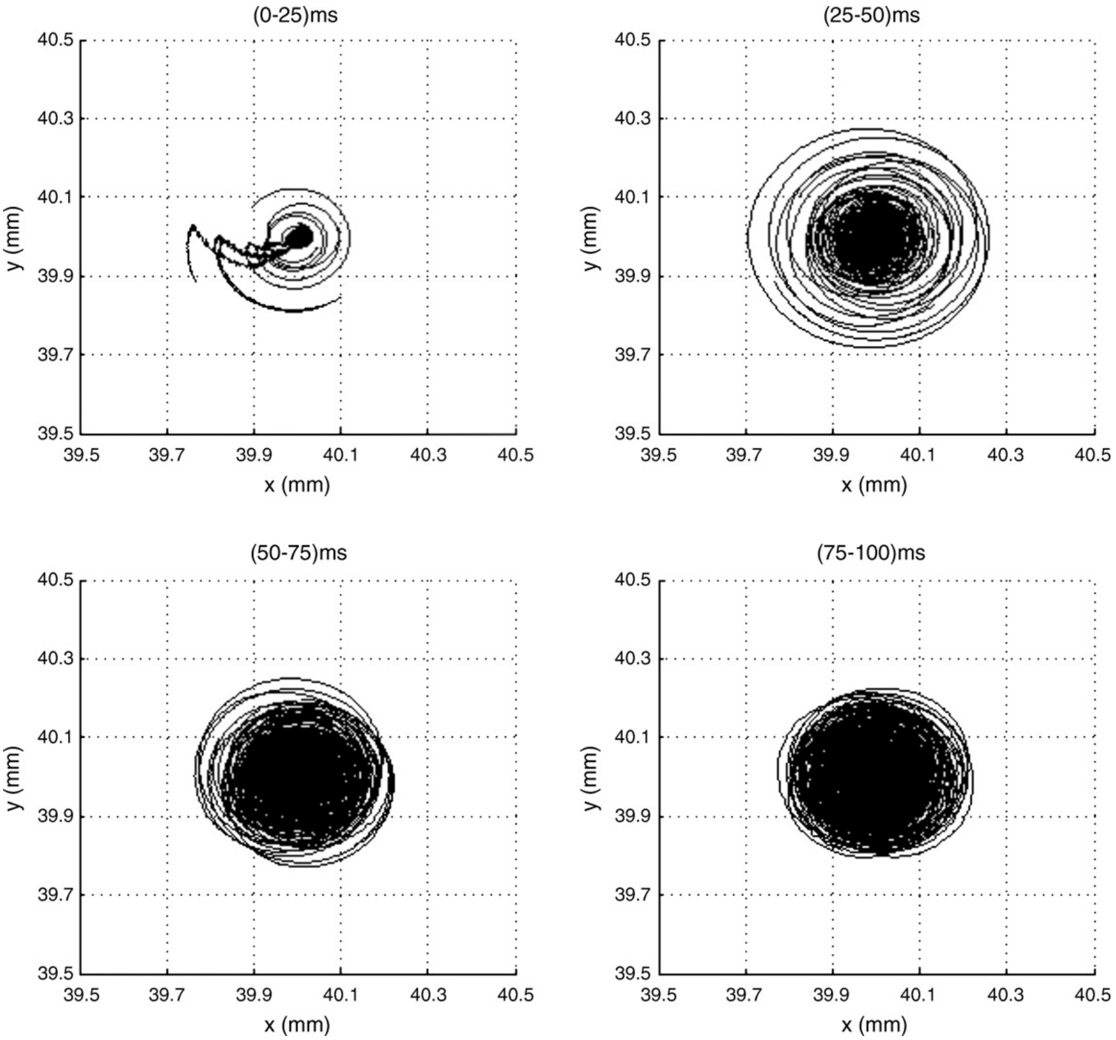

Fig. 21. Radial *xy* view for the trajectories of 25 thermal negative ion clouds ($m/z = 146$) after consideration of columbic repulsion and collisional damping in the time range 0–100 ms in the potential configuration −3/3/0/3/−3 of the new cell.

4×10^{-16} C to represent nearly 2000 positive and 2000 negative ions.

Axial trajectories of central positive ions and terminal negative ions as a function of time in the range 0–800 ms are shown previously in Fig. 2 in the potential configuration −3/3/0/3/−3. All ions have thermal kinetic energy of 4×10^{-2} eV in the *z*-direction. Positive ions cool down axially to the central region C of the ICR cell, where a flat well exists. Negative ions cool down to the terminal sites of detection regions (B and D), where two terminal potential hills for trapping negative ions exist. This ion cooling process occurs in the first 100 ms. No electrons were simulated, since the experimental sequence was such that all electrons were attached to SF_6 at this time. Due to the flat central region of the electric field shown in Fig. 1, positive ions have larger trapping amplitudes than the negative ions.

At a potential configuration of −3/3/0/3/−3 there is a gap of nearly 5 mm between the maximum trapping amplitudes of central positive and terminal negative ions as shown in Fig. 2. A 500 ms square waveform pulse of 16 kHz frequency (with amplitude of 2 Vp-p) is capable to establish an axial overlap between central positive and terminal negative ions (Fig. 12). After the end of this pulse, ions of both polarities cool down axially to their stable regions as shown after 600 ms.

This ion–ion overlap is due to the increase of the trapping amplitude of negative ions during excitation. They oscillate continuously between regions B and D, whereas positive ions are still confined in the central region (C) of the ICR cell. Small positive ion loss is shown in Fig. 12 in the first 100 ms of the axial RF pulse.

Fig. 13 describes axial ion motion due to an axial square waveform pulse with frequency of 100 kHz. This axial pulse is also triggered between 100 and 600 ms. We notice the RF-driven motion of the terminal negative ions toward the inner central region of the cell during the whole duration of the axial RF pulse. This motion is initiated after some negative ion change from B to D in the first 5 ms at the beginning of the axial RF pulse. After the end of the axial RF pulse, negative ions shift to their initial terminal stability regions (B and D) as seen before.

At this point, the following question is worth to be asked: Why were neutralization reactions not observed, although ion–ion overlap does occur, when an axial square waveform at 16 kHz is triggered as shown above?

The ion densities in ICR experiments are lower compared to flowing afterglow or quadrupole ion trap experiments. This should give lower but detectable reaction yields. As an important requirement for ion–ion reactions in ion traps, we have decided to study the radial confinement of thermal ions inside this ICR cell in the

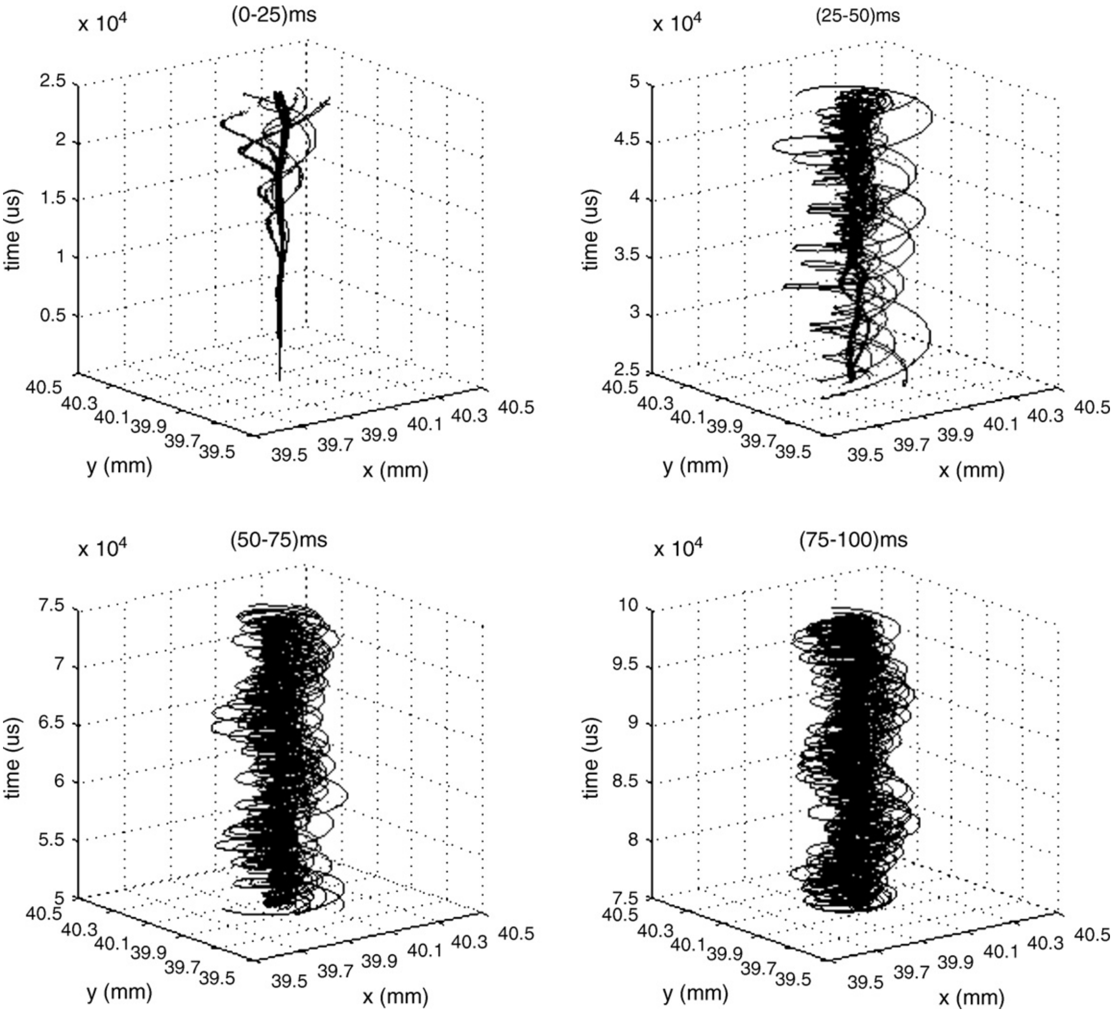

Fig. 22. A 3D radial view of Fig. 21.

double hill potential configuration −3/3/0/3/−3, which was used experimentally before and to compare it with a standard closed cylindrical ICR cell with the same detection length and inner diameter, operated at a simple potential configuration of 3/0/3 for positive ions and −3/0/−3 for negative ions.

From Fig. 14, it is clear that axial confinement within the equipotential lines marked with 0.6 V will exist for positive ions trapped in this ICR cell, since the central region has a potential of 0.55 V.

Figs. 15 and 16 describe radial confinement of 25 thermal positive ($m/z = 127$) in 3/0/3 in the simple closed cell shown in Fig. 14. Figs. 17 and 18 show ion trajectories of 25 thermal negative ($m/z = 146$) ion clouds in the single section ICR cell in the potential configuration −3/0/−3. Each simulation was run for a total columbic charge of 2×10^{-16} C (nearly 2000 ions) and a collisional damping constant of 1×10^{-4}.

As shown from Figs. 16 and 18, a simple normal magnetron motion for both ion polarities is obvious in these simulations. If we take a look on the radial confinement of the same number of thermal positive and negative ion clouds in the new open cylindrical ICR cell, whose equipotential lines are seen in Fig. 1, we will notice a significant difference, although all simulations were run with the same flight parameters and the same user program, which simulates collisional damping and axial RF pulses (when activated).

Fig. 19 shows an abrupt increase in the magnetron radius of positive ions. Furthermore, the magnetron radius is larger than that for a normal closed cylindrical ICR cell (compare it with Fig. 15). Magnetron trajectories of thermal positive ions, trapped in the center of the detection region (C) of the new ICR cell, are very large, with zero probability of trajectories in the center region (Fig. 19). In contrast to this observation, this effect is not found for thermal negative ions (Fig. 20). So how do negative ions fly on the radial plane in the new ICR cell?

In order to simplify the trajectories, we have decided to look at smaller time segments (25 ms each) in the first 100 ms of ion flight. The results are shown in Fig. 21. The upper left diagram looks strange, but it confirms the fact, that what is seen in the upper right diagram of the same figure (time segment 25–50 ms) is not due to a radial expansion of the magnetron radii of all negative ions.

A 3D radial view of Fig. 21 is shown in Fig. 22. Each diagram in Fig. 22 explains what was being seen in Fig. 21. Thermal terminal negative ions have different magnetron radii.

As seen from Fig. 23, all positive ion clouds remain together and they follow their magnetron trajectories as a bundle. The duration of one magnetron cycle is 75 ms, and this means almost 13 Hz for their magnetron frequency. This is a very low frequency compared with magnetron frequencies of ions trapped in simple closed ICR cells (>60 Hz). In addition, magnetron frequency of terminal negative ions is noticeably higher than that of central positive ions.

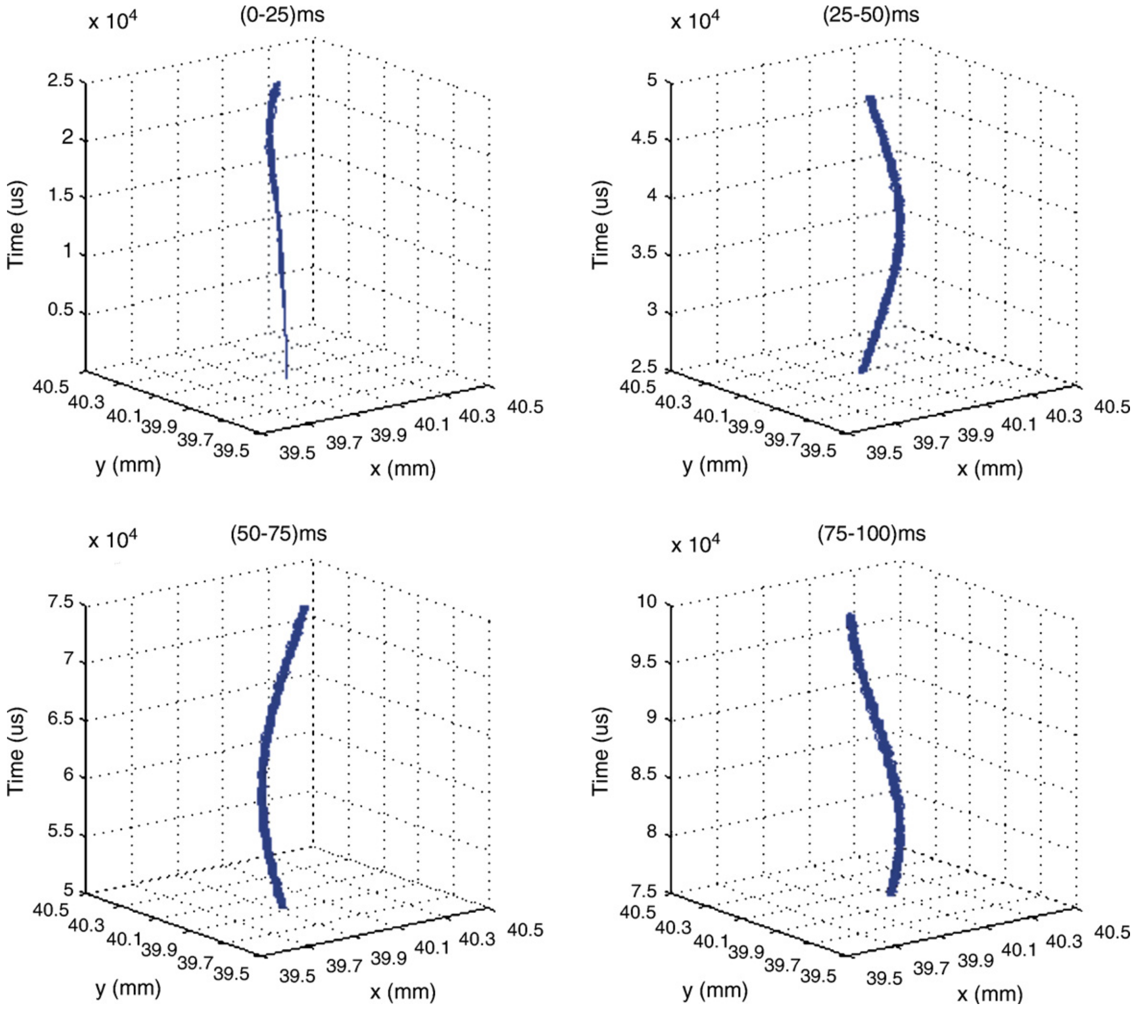

Fig. 23. 3D radial view of the ion trajectories of 25 positive ion clouds $m/z = 127$ in four time segments in $-3/3/0/3/-3$ of the new cell.

It is interesting to know why thermal terminal negative ions have different radii, as shown in Fig. 20 before. Let us examine first the potential distribution in the *yz* cross-section which intersects the cell in the middle ($x = 40$ mm). This potential distribution is shown for the detection region in Fig. 24. The third dimension, the range of potentials, is color coded (in the online version of the paper).

Along the vertical line defined by $z = 100$ mm there is a potential maximum at $y = 40$ mm (the central point in the detection region). Along the horizontal line defined by $y = 40$ mm, there is a double hill potential, caused by the applied potential configuration $-3/3/0/3/-3$. In regions of low potential the effective potential approaches -2 V at the left and right margins of the detection region as the tube electrodes A and E are approached (points (72, 40) and (129, 40)). At the outer circumference of the side electrodes the potential approaches +3 V, as expected.

Fig. 24B shows a finer potential distribution within the potential range from -1 to $+1$ V. A terminal negative ion, generated on axis in $z = 83$ mm vibrates axially in the region z (81–90 mm). The radial potential configuration in the planes from $z = 81$ to 90 mm undergoes a remarkable inversion (see below).

To simplify, the radial potential and electric field configurations at $z = 83$, 100, and 117 mm are shown in Figs. 25–27, respectively. Note the identity in the potential and electric field pattern in Figs. 25 and 27 acquired at $z = 83$ and 117 mm, respectively. This is due to the symmetry in the ICR cell.

The normal radial potential pattern in classical ICR cells is a parable with a local maximum in the center for a single axial electric potential well. This is true only in the central region of this new ICR cell, cf. Fig. 26 for $z = 100$ mm. The radial electric field component on the same figure has a negative slope and is zero in the center at $y = 40$ mm. An increase of absolute values is seen if deviation from $y = 40$ mm occurs. Thus, central positive ions move radially outward.

On the other hand, the radial potential distribution on the terminal axial regions, for example $z = 83$ and 117 mm, shows double hill potential configuration with local minimum in the center at $y = 40$ mm. In addition, the radial component of the electric field has a positive slope in the region y (33–47 mm). This indicates an outward oriented radial force, which pushes the negative ions toward the terminal potential hills at $y = 28$ and 52 mm, where global radial potential maxima exist.

If we return back to Fig. 24B, we see that the large variation in the radial potential patterns in the narrow axial stability regions for negative ions z (81–90 mm) and z (110–119 mm), is responsible for the large radial spread in negative ion motion on the *xy*-plane as shown in Fig. 22 before.

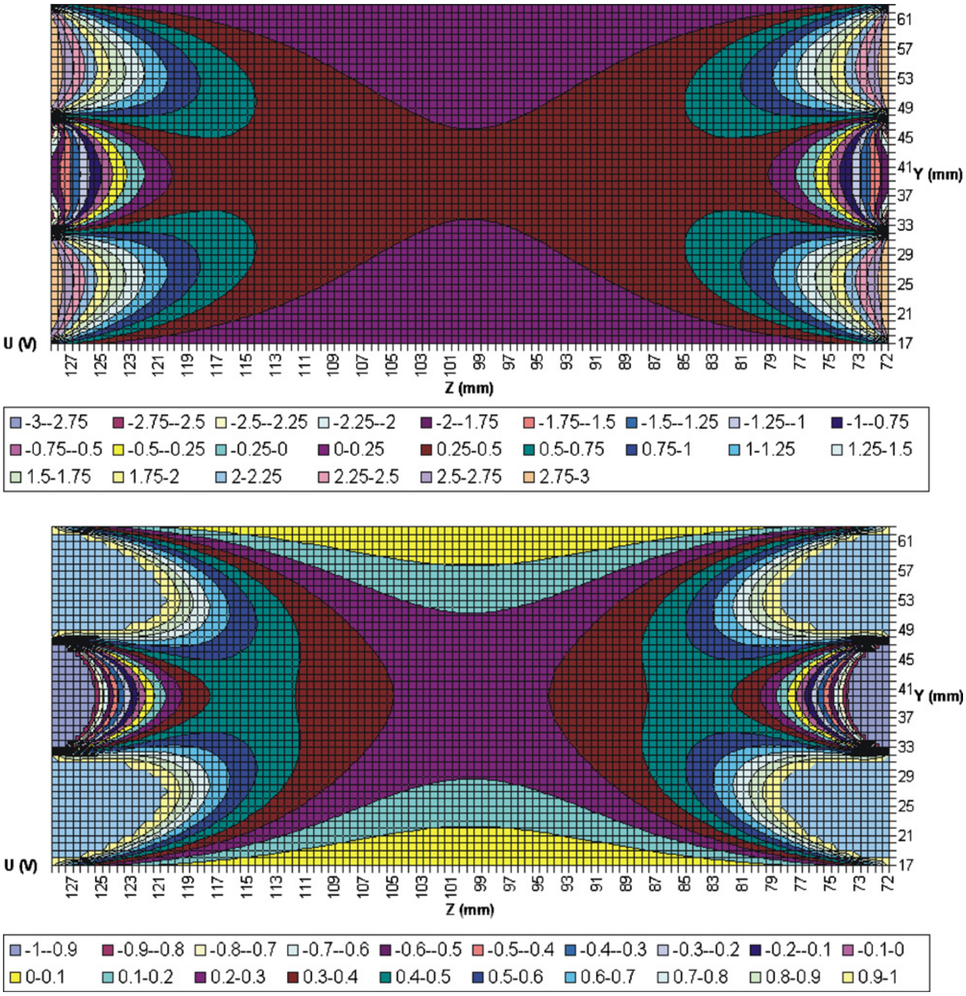

Fig. 24. *Top*: *yz*-midplane card, which shows the potential distribution in the detection region with configuration −3/3/0/3/−3 of the new open cylindrical ICR cell. *Bottom*: Potential distribution on *yz*-midplane in the detection region with finer potential ranges. Corners, which lie closest to the side electrodes have higher potentials, than +1, and cannot be identified in this figure due to the potential limit (−1 to +1 V) applied for this view.

The large variation in the radial potential patterns in the range *z* (81–90 mm) is shown in Fig. 28. Note in Fig. 28 that the potential pattern changes from a sharp double hill potential to a simple mono hill curve as the negative ions move axially a few millimeters in their terminal stability region from $z = 81$ to 89 mm. Subsequently, outward radial electric forces with different amplitudes can be deduced from Fig. 28.

Now let us discuss the radial motion of thermal central positive and terminal negative ions under the influence of the axial square waveform RF pulse of frequency 16 kHz, used before, since we have noticed from Fig. 12, that this pulse at this frequency is capable to provide an axial ion–ion overlap in the central region of the ICR cell, when the potential configuration −3/3/0/3/−3 is used.

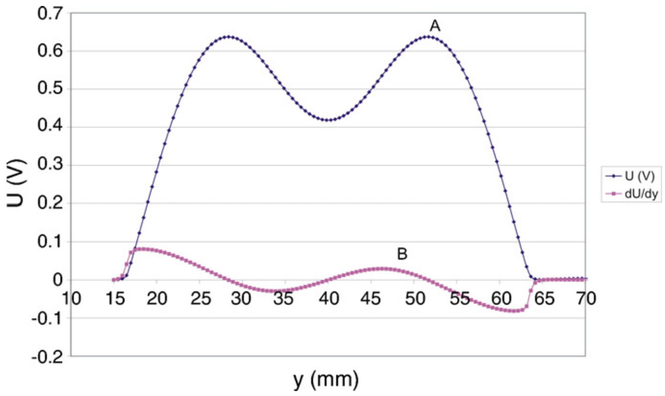

Fig. 25. Distribution of (A) radial potential (V) on $z = 83$ mm plane and (B) radial component of the electric field in *y*-direction (V/mm) as a function of the radial distance *y*. Center potential is located on $y = 40$ mm.

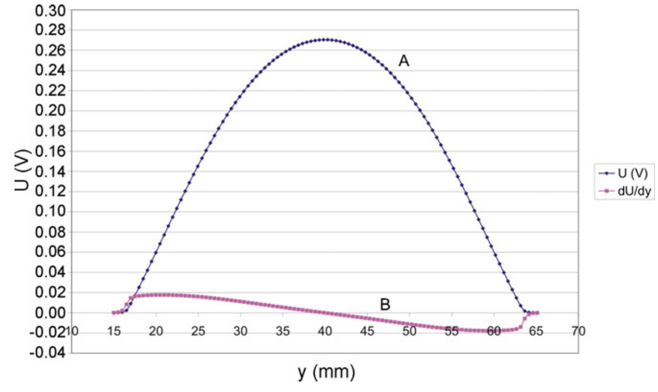

Fig. 26. Distribution of (A) radial potential (V) on $z = 100$ mm plane and (B) radial component of the electric field in *y*-direction (V/mm) as a function of the radial distance *y*. Center potential is located on $y = 40$ mm.

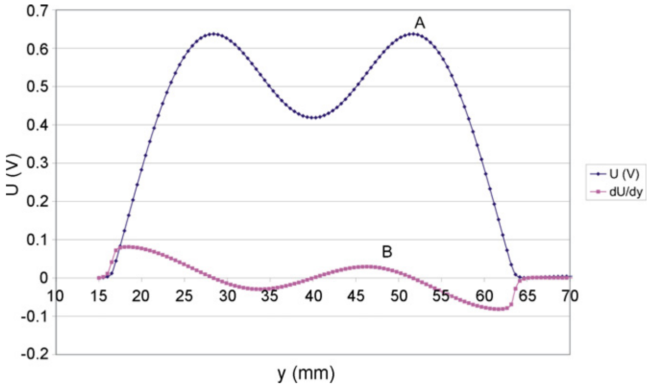

Fig. 27. Distribution of (A) radial potential on $z = 117$ mm plane (V) and (B) radial component of the electric field in y-direction (V/mm) as a function of the radial distance y. Center potential is located on $y = 40$ mm.

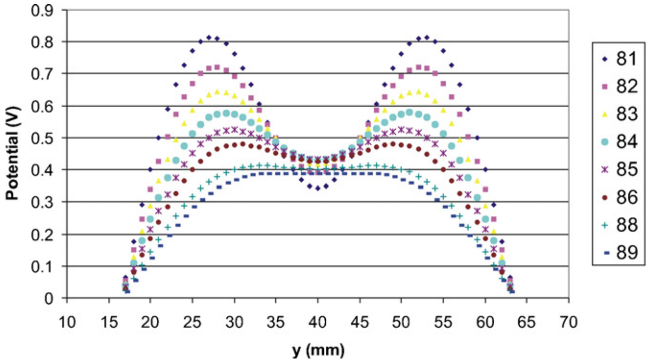

Fig. 28. Radial potential distribution at different Z values (shown in the legend in mm) in the potential configuration −3/3/0/3/−3 of the new ICR cell. These Z values shown in the legend represent a terminal stability region for trapping negative ions. Center potential is located on $y = 40$ mm.

Fig. 29 shows the radial trajectories of 25 positive ($m/z = 127$) and 25 negative ($m/z = 146$) ion clouds as a function of time, when an axial RF pulse with square waveform of frequency 16 kHz is triggered after 100 ms for further 25 ms.

Detailed analysis of the left diagram in Fig. 29 shows no radial interaction between negative ions (black) and positive ions (grey). However, in the time interval 75–100 mm there is no axial ion–ion overlap, since the RF square waveform pulse at 16 kHz is not triggered. The right diagram in Fig. 29 shows ion–ion radial proximity in the time range 100–125 ms, where the ion–ion axial overlap takes place (Fig. 12) due to the activity of the square waveform pulse at 16 kHz, which is applied on both side electrodes in phase. In spite of this axial and radial interaction in the time range 100–125 mm, a large deformation in the negative ion trajectories can be seen in the right diagram of Fig. 29. In addition, some anions turn around in front of the cloud of positive ions without collision. So ion focusing must be sustained if effective collisions are to be guaranteed. This was not possible with this design and the RF square waveform operation mode employed. The SIMION simulations provide an explanation for the absence of ion–ion neutralization reactions.

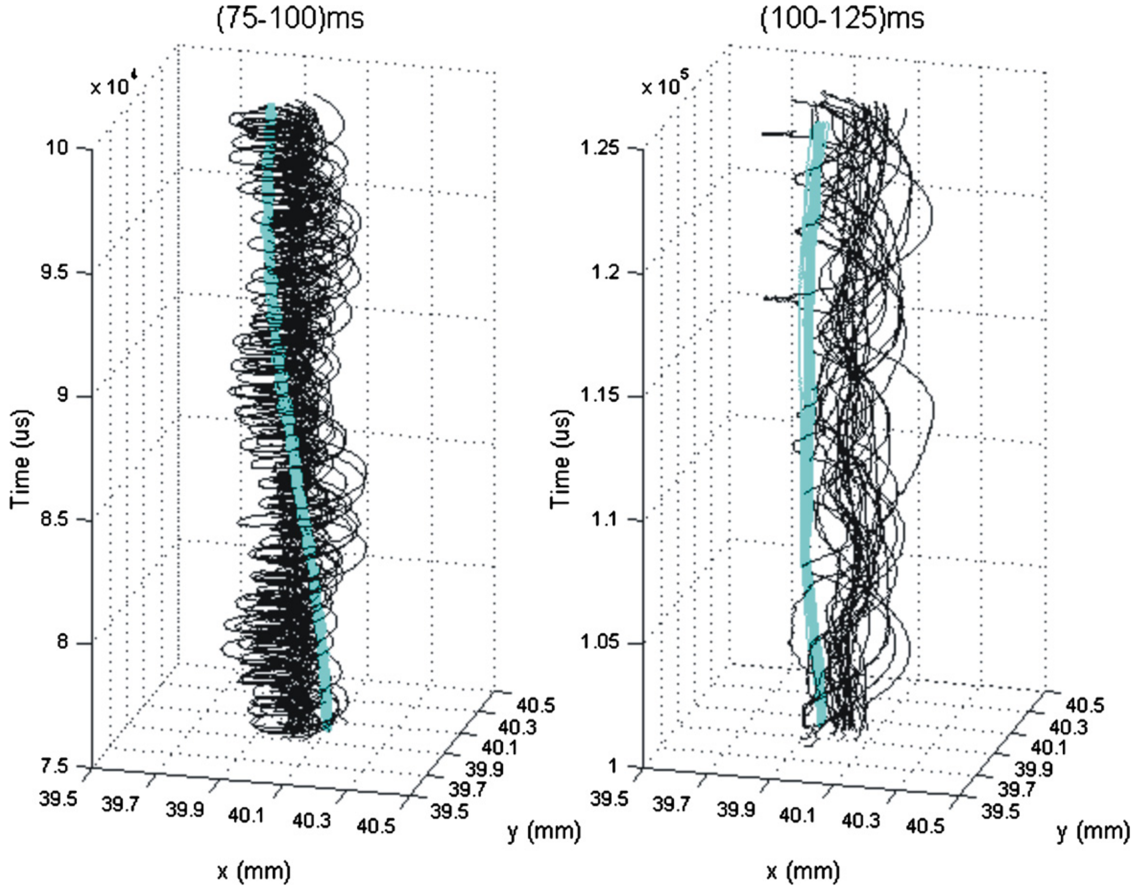

Fig. 29. 3D view of 25 positive and 25 negative ion clouds in the range 75–100 ms without axial RF pulse (left) and with axial RF square waveform pulse of frequency 16 kHz in the range 100–125 ms (right). Potential configuration −3/3/0/3/−3 of the new ICR cell is used.

4. Conclusion

A new ICR cell has been designed to trap simultaneously positive and negative ions in different spatial regions in the detection region along the *z*-axis. Therefore both ion polarities can be detected without loss of sensitivity. The optimum potential configuration of −3/3/0/3/−3 has been studied in detail. Excitation of the trapping motion causes overlap of the trajectories of both ion polarities. Since a static potential configuration is not able to sustain an axial ion–ion overlap, several axial RF electric fields at different frequencies, durations, and waveforms have been implemented to establish the overlap. Long-range ion–ion interactions have been experimentally observed, with a sinusoidal axial RF pulse, whose frequency is in resonance with the trapping frequency of the central positive ions. Use of square waveform pulses of frequency of 16 kHz are not sufficient for an effective ion–ion overlap, although some axial ion–ion overlap was established. Simulations of radial and axial potential configurations were employed to explain the absence of ion–ion reactions.

Acknowledgements

B. Kanawati would like to thank FCI (Fonds der Chemischen Industrie) for a PhD grant. We also thank Mr. Wolfgang Fulda and his coworkers in the mechanical shop, who realized the new ICR cell design and provided continuous mechanical support.

References

[1] A.G. Marshall, C.L. Hendrikson, G.S. Jackson, Mass Spectrom. Rev. 17 (1998) 1.
[2] S. Guan, A.G. Marshall, Int. J. Mass Spectrom. 146/147 (1995) 261.
[3] Y. Wang, K.P. Wanczek, Rev. Sci. Instrum. 64 (1993) 883.
[4] V.H. Vartanian, D.A. Laude, Org. Mass Spectrom. 29 (1994) 692.
[5] R. Malek, K.P. Wanczek, Rapid Commun. Mass Spectrom. 11 (14) (1998) 1616.
[6] V. Frankevich, R. Zenobi, Int. J. Mass Spectrom. 207 (2001) 57.
[7] M.V. Gorshkov, S. Guan, A.G. Marshall, Rapid Commun. Mass Spectrom. 6 (1992) 166.
[8] S. Guan, M.V. Gorshkov, A.G. Marshall, Chem. Phys. Lett. 198 (1–2) (1992) 143.
[9] M.J. Church, D. Smith, Int. J. Mass Spectrom. 23 (1977) 137.
[10] D. Smith, M.J. Church, Int. J. Mass Spectrom. 19 (1976) 185.
[11] J.R. Peterson, W.H. Aberth, J.T. Moseley, J. Roger Sheridan, Phys. Rev. A 3 (5) (1971).
[12] W. Schön, S. Kründener, F. Melchert, K. Rinn, M. Wagner, E. Salzborn, Phys. Rev. Lett. 59 (14) (1987) 1565.
[13] W. Aberth, J.R. Peterson, D.C. Lorents, C.J. Cook, Phys. Rev. Lett. 20 (1968) 979.
[14] A. Diel, H. Bräuning, R. Trassl, D. Hathiramani, A. Theiß, H. Kern, E. Salzborn, I. Hofmann, J. Phys. B: Atom. Mol. Opt. Phys. 34 (2001) 4073.
[15] S.J. Pitteri, S.A. McLuckey, Mass Spectrom. Rev. 24 (6) (2005) 931.
[16] S.A. McLuckey, J.L. Stephenson Jr., Mass Spectrom. Rev. 18 (1999) 83.
[17] S.A. McLuckey, J.L. Stephenson, Mass Spectrom. Rev. 17 (6) (1998) 369.
[18] SIMION Version 7, D.A. Dahl, Idaho National Engineering and Environmental Laboratory, Idaho Falls, ID, 2005.
[19] B. Kanawati, K.P. Wanczek, Rev. Sci. Instrum. 78 (2007) 074102.
[20] D.A. Dahl, User's Manual of SIMION, Idaho National Engineering and Environmental Laboratory, Idaho Falls, ID, 2005.
[21] B. Kanawati, K.P. Wanczek, Int. J. Mass Spectrom. 269 (2008) 12–23.